# SCOLIOSIS VISUALIZATION USING ULTRASOUND DATA

by

Benjamin David Church

A thesis submitted to the School of Computing

In conformity with the requirements for

the degree of Master of Science

Queen's University

Kingston, Ontario, Canada

April, 2018

# Abstract

Scoliosis is a disease characterized by spinal deformation which typically appears during adolescence and growth. Regular assessment to monitor the progression of the disease is important to ensure timely intervention. Routine assessment is performed with X-ray but other techniques are used for preliminary screening or advanced assessment. The limitations of various imaging modalities leave a need for a method for producing 3D patient-specific spinal visualizations suitable for scoliosis assessment using ultrasound imaging. This thesis presents a collection of techniques which, taken together, constitute such a method. After exploring the related background material, a method for producing visualizations from ultrasound-accessible skeletal landmarks is presented. The method uses the transverse process locations to deform a healthy-shaped spine model to match patient anatomy. Visualizations were generated and compared to CT to validate the method. Subsequent developments to the ultrasound assessment process were aimed at reducing operator interaction by automatically segmenting the spine from ultrasound, and generating landmarks to use with the visualization method. A bone segmentation method recently integrated into PLUS[1] was used to identify the bone surfaces in ultrasound scans. Then a variation on *k*-means estimates the landmark locations. Automatically generated landmarks are prone to containing defects, so a Slicer[2] module offering various correction operations was developed. An ultrasound scan was used to produce a visualization with automatically generated, and subsequently repaired, landmarks. Initial results demonstrate the challenges of automatically generating 3D spinal visualizations from ultrasound data. Landmarks are essentially an under-sampling of a segmentation, and degrade results through a loss of information. Furthermore, operator controlled reparation operations reintroduce user interaction. There is still promise in the overall workflow. The landmark-based visualization method has been used in published work, and modular and incremental developments may improve segmentation generation and interpretation.

[1] http://plustoolkit.org/
[2] http://slicer.org/

# Co-Authorship

The work presented in this thesis was completed under the supervision and guidance of Dr. Gabor Fichtinger, Dr. Parvin Mousavi, and Dr. Tamas Ungi. This work appears in the publication:

- B. Church, A. Lasso, C. Schlenger, D. P. Borschneck, P. Mousavi, G. Fichtinger and T. Ungi, "Visualization of scoliotic spine using ultrasound-accessible skeletal landmarks," in *Proceedings of SPIE*, Orlando, 2017 [1].

# Acknowledgements

First, I would like to thank my supervisors, Dr. Gabor Fichtinger and Dr. Parvin Mousavi. Your continuous feedback on my work has made me a better researcher, writer, and student. Most importantly, both of you believed in me and this work, even when I did not. Thank you both for your guidance and supervision, without which I would surely have been lost trying to navigate the world of research.

I would also like to thank Dr. Tamas Ungi. Tamas, your endless technical and academic guidance have given me direction throughout the course of this degree. Thank you for providing the insight and foresight needed to steer my work in productive and meaningful directions.

Finally, I would like to thank my friends and family. Without your constant love and support, nothing I have done would have been possible. Thank you all for making everything possible and worthwhile.

# Table of Contents

# List of Figures

# List of Tables

# Glossary

**2D** Two-dimensional

**3D** Three-dimensional

**Apical vertebra** The most displaced vertebra in a scoliotic curve

**B-mode** Brightness-mode

**BMI** Body mass index

**Cobb angle** The angle between the end plates of the end vertebrae

**CT** Computed tomography

**DRR** Digitally rendered radiograph

**End vertebrae** In scoliosis, the two vertebrae with the greatest coronal angle between their endplates

**mm** Millimeter

**MRI** Magnetic resonance imaging

**s** Second

**T** Tesla, a unit measuring magnetic field strength

# Chapter 1

# Introduction

## 1.1 Scoliosis

Scoliosis is a disease of the spine characterized by coronal curvature and associated with 3D deformation. Adolescent idiopathic scoliosis is the most common variety of the disease, affecting 1-5% of the population [2]. It is usually diagnosed during early adolescence, and the curvature progresses until growth ceases. The gold-standard of assessment for diagnosis and treatment planning is measurement of the Cobb angle from a radiograph of the torso in the coronal plane. The Cobb angle is defined as the maximum angle between the endplates of any two vertebrae [3], measured in the coronal plane, as illustrated in Figure 1.

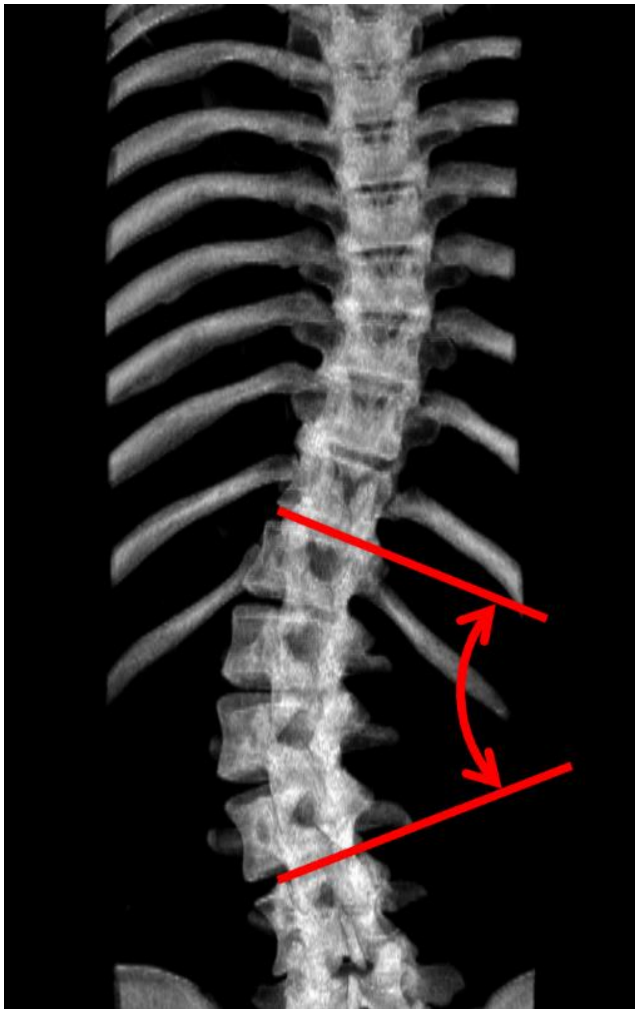

**Figure 1: DRR illustrating the Cobb angle, a measure of scoliotic deformity**

The progressive nature of the disease requires regular assessment to ensure that patients receive less invasive treatments when possible. Bracing has been shown to be effective at slowing or halting the curvature progression in mild to moderate cases, or Cobb angles between 20° and 40° [4]. Surgical vertebral fusing may be necessary to stabilize spines with Cobb angles exceeding this range. As some lateral curvature of the spine is normal, a Cobb angle of 10° is the threshold for diagnosis [3].

Symptoms of the disease are largely the result of deformation of the torso; these symptoms may include psychological effects arising from cosmetic aberration, back pain, and impaired balance or respiratory function if the deformation is allowed to progress.

To assist with the interpretation of the anatomy, a short description of sites of interest on the vertebrae and visualization planes are shown below. Two vertebrae, the repeating skeletal units which form the spine, are shown in Figure 2.

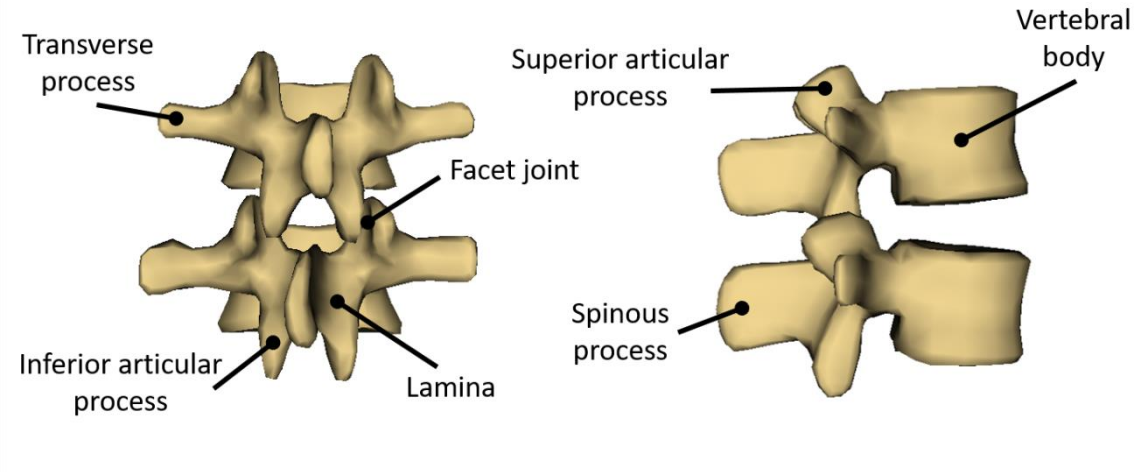


**Figure 2: (Left) – Posterior view of vertebral anatomy (Right) – Right view**

The vertebrae have two symmetries: bilateral and axial. Bilateral symmetry is the right-left similarity, and axial symmetry is the similarity of neighboring vertebrae. The vertebrae lack a third symmetry, about a coronal plane, in that the posterior processes do not resemble the vertebral bodies. The anatomic planes, which define the anatomic directions, are shown in Figure 3. A parasagittal plane is shown in yellow. Its surface normal are the right-left directions. The red plane is axial, its surface normal are the superior-inferior directions. A coronal plane is shown in green. The anterior-posterior directions are normal to this anatomic plane.

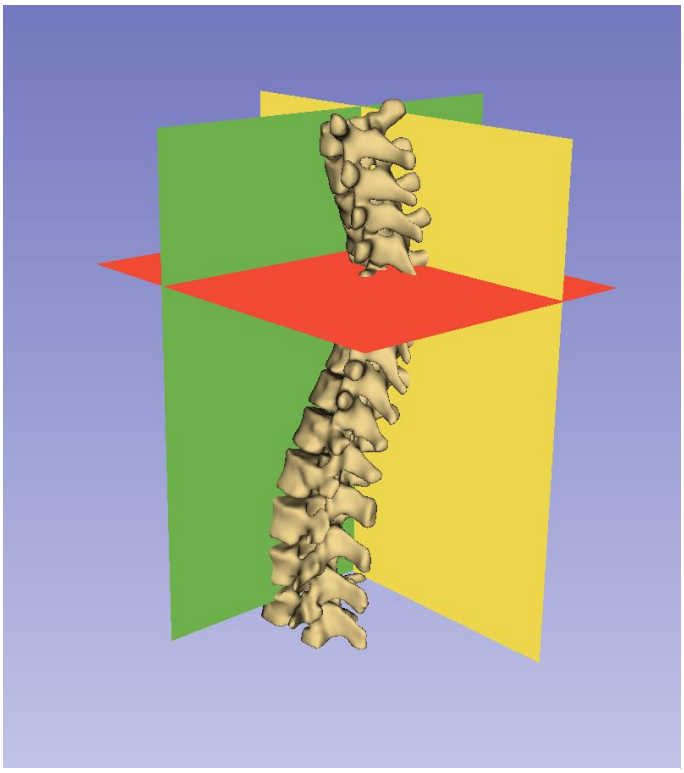

**Figure 3: Anatomic planes shown with spine CT. Green plane is coronal, yellow is parasagittal, and red is axial.**

### 1.2 Visualization for therapy

Visualization of scoliosis is important for ensuring optimal care through proper assessment. X-ray imaging remains the gold-standard for assessment and monitoring because it produces a full posterior view of the spine, suitable for scoliosis quantification via the Cobb angle. Although planar assessment of the spine is useful for measuring curvatures, it is limited in the information it provides regarding 3D aspects of deformation. The modes of deformation are defined in terms of the rotation of vertebrae about the surface normals of the three anatomic planes. Vertebral rotation, as a deformation, is rotation about the axis of the vertebrae, the superior-inferior direction. Lordosis and kyphosis are curvatures in the spine about a right-left axis, of a sagittal plane. Scoliosis is curvature about an anterior-posterior axis, of the coronal plane. To assess vertebral rotation, or anterior-posterior deformation of the spine such as lordosis, patients may be referred for additional imaging [5]. In a hospital setting, the additional imaging may come from another X-ray, this time in the lateral plane, or more sophisticated methods like MRI or CT.

The importance of visualization is not limited to the decision of whether to prescribe a brace or perform surgery. Practitioners providing conservative treatment in the form of physical therapy or chiropractic care may also wish to tailor the treatment to the patient-specific conditions [6]. Several established chiropractic or physiotherapeutic methods, such as the Schroth [7] and Dobosiewicz [8] methods, require 3D

information about the patient spinal anatomy. The Schroth method involves directing the patient to perform 'rotational breathing' which opposes the torsion imposed on the torso by scoliotic deformation to improve respiratory function and posture [9]. The Dobosiewicz method augments asymmetric breathing exercise with proprioceptive and exteroceptive facilitation at the apical vertebra [8]. The directionality of asymmetric breathing or manual therapy depends on the direction of the scoliotic curvature in 3D, not simply the magnitude of the Cobb angle. Visualization in these settings is especially challenging since even X-ray may be unavailable, and surface-based assessment methods like the Scoliometer and optical techniques provide limited information about internal structure.

The risks associated with repeated exposure to ionizing radiation during adolescence have caused some controversy regarding the use of radiographic method for scoliosis monitoring. Monitoring protocols may provide some reduction in radiation exposure. Radiographic assessment may be performed less frequently in mild or slowly progressing cases, and MRI may be employed for 3D assessment instead of CT. Nonetheless, ionizing radiation still conveys increased cancer risks [10], especially with respect to breast cancer in women [11], and is not available in physiotherapeutic or chiropractic settings. MRI is not a potential replacement for radiographic assessment because of its cost and availability. Hospital-based assessment and monitoring, and therapeutic settings both stand to benefit from an accessible system capable of providing 3D visualization of scoliosis, without using ionizing radiation. Ultrasound imaging offers just such a solution. It does not use ionizing radiation, making it safe and thereby inexpensive and accessible. Other instruments and imaging modalities have their respective uses and limitations, but we believe tracked ultrasound to be the best available solution for the requirements.

### 1.3 Objective

The objective of this thesis is to develop a method for 3D visualization of the spine suitable for scoliosis assessment. The method must use tracked ultrasound data to ensure availability and complete radiation safety.

## 1.4 Contributions

The main contributions of this thesis are:

- A method for generating patient-specific 3D spinal visualizations using a thin-plate spline transform to realistically deform a healthy-shaped model to patient ultrasound data.
- A technique was designed for this visualization method, which supplements natural landmarks with anchor points, ensuring that the registration has sufficient 3D constraint.
- Validation of the visualization method for depicting scoliotic deformities.
- A method for automatically generating the landmarks used by the visualization method from an ultrasound scan. This was done to minimize operator interaction in manual landmark identification.

Contributions regarding the visualization method are addressed in Chapter 3. Chapter 4 describes the automatic landmark generation. These chapters are presented in the order in which their subject material was developed rather than the order in which it is employed for data processing. Their relation, through the workflow that is the sum of Chapters 3 and 4, is shown in Figure 4. The patient presents for scoliosis assessment and a spatially tracked ultrasound is performed. The bone surfaces are automatically segmented from the ultrasound images, and rendered as a 3D volume. This volume depicts only the bones visible in ultrasound and does not resemble a spine yet. An algorithm automatically estimates the locations of bilateral skeletal landmarks from the segmentation and the user corrects defects in the landmarks with operations offered in a Slicer module. These landmarks are then used to register a healthy-shaped model to the patient's anatomy with a thin-plate spline. The deformation imposed on the healthy-shaped model by the thin-plate spline results in a 3D, patient-specific spinal visualization suitable for depicting scoliotic deformation.

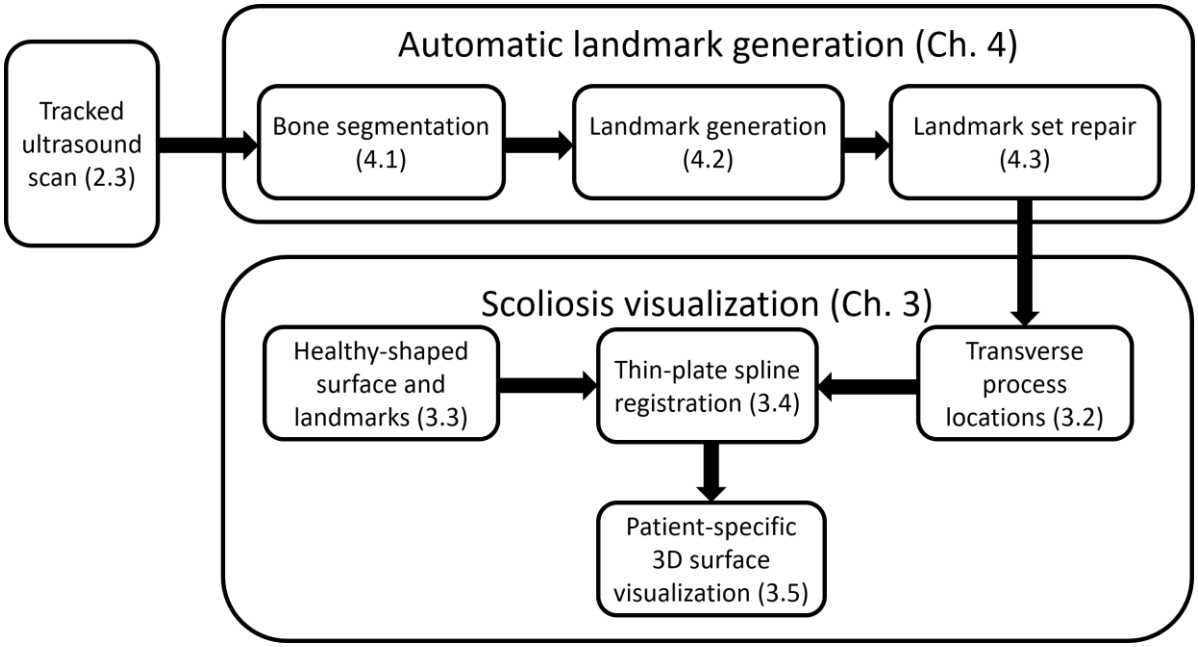


**Figure 4: Chapters', and their sub-sections', combined sequence for visualization from ultrasound data**

# Chapter 2

# Background

Scoliosis is classified into varieties, depending typically on the age of the patient. In fact, the various diagnoses allow for spinal deformity at any age. These range from congenital scoliosis at the beginning of life, to adult degenerative scoliosis when the spine wears out. Congenital scoliosis describes deformation present at birth [12]. Its immediate cause is usually a developmental defect in one or more vertebrae. Vertebrae may be wedge shaped, not properly segmented from neighboring ones, or missing entirely. The geometric perturbation introduced by such a defect can cause abnormal curvature in the overall structure of the spine during growth, if not corrected. Adult degenerative scoliosis is, by definition, deformation resulting from deterioration of the spine. Coronal curvature can result from asymmetric deterioration of the spine, often occurring at the facet joints. The deterioration may be the result of metabolic disorders in the bones, disk degeneration, or misalignment of the pelvis [13]. Changes in bone properties can also cause changes in the structures of the vertebral bodies, compressing them. Compressed vertebral bodies, often accompanied with disc degeneration, either normal or pathological, can cause kyphotic deformation of the spine [14]. That is, curvature about a right-left axis into the anterior direction. This is commonly seen as a stooped head or hunched back in old age. Degenerative scoliosis is unlikely to go undiagnosed as deterioration of bones and joints causes patients to present with potentially severe back pain. Congenital and degenerative scoliosis may have opposing causes, in that congenital scoliosis becomes a deformity when an initial defect is magnified by growth while degenerative scoliosis is the result of deterioration. However, their common result is deformation of the patient's spine and torso.

The most common variety, however, is adolescent idiopathic scoliosis, affecting 1-5% of the population [2]. Idiopathic scoliosis, by definition, refers to the cases for which no cause is known. Results from a study of over 60,000 twins suggest that genetics are often a factor in causing the disease, but that environmental effects are more important [15]. It is usually diagnosed after a parent notices asymmetry in the child's back,

such as uneven scapulae or a rib hump. Public scoliosis screening programs have been investigated and implemented in some American states [16]. Screening methods employ various tools, each with their limitations with respect to scoliosis assessment, discussed in their respective subsections below. These limitations are why these screening tools are used for detection, rather than for diagnosis or assessment of the disease.

## 2.1 Detection and screening

Unlike adult degenerative scoliosis which presents itself with back pain, adolescent idiopathic scoliosis may develop without indicative symptoms. The disease is usually detected by parents or family doctors once deformation of the spine has progressed to the point of causing externally visible asymmetry in the torso. This is one of the principal points driving research in public scoliosis screening programs on the adolescent population. The debate regarding the costs and benefits of screening programs is years old and ongoing [17]. Proponents argue that earlier detection can lead to earlier diagnosis and treatment when necessary. Critics point out the screening methods' high false-positive rates and the costs incurred to healthcare systems arising from many unnecessary referrals. The following subsections describe three common approaches to scoliosis detection with reference to their utility for public screening.

### 2.1.1 Observation and palpation

Despite the development of numerous technologies to make scoliosis screening quantitative, more accurate, and improve its sensitivity and specificity, the simplest methods remain the most popular. Examination for scoliosis often begins with simple observation of the shirtless patient. Differences in limb length, shoulder or hip height, or asymmetry in the back can indicate scoliosis. The Adam's forward bend test, often simply called the 'forward bend test', then places the patient in a posture assess torso rotation [18]. The patient bends forward until their back is horizontal. This increases the prominence of an asymmetric rib hub and gives the clinician a perspective to easily see it. The forward bend test makes the decision to refer a patient for diagnosis based on human judgement. The test, by itself, is generally not recommended for public

screening programs [19]. Screening assessment sensitivity and specificity can be improved by combining the forward bend test with instrumental techniques [20].

### 2.1.2 Scoliometer

A Scoliometer is an instrument which measures the angle of axial tilt rotation at some section across the torso. Like a carpenter's level, traditional Scoliometers use a bubble or enclosed ball that is observed against a protractor to indicate the angle. More recently, the function has been implemented on smartphones using their built-in accelerometers to measure inclination [21] [22]. The traditional Scoliometer and its smartphone-based variety are shown in Figure 5. Scoliometer screening is performed with the patient bending as far forward as they can. Axial rotation angles are measured from one end of the torso to the other, and the single greatest angle is noted. Huang reported difficulties in selecting an optimum angle cutoff for referral [23]. The Scoliometer is not a sensitive detector of Cobb angles up to 20°; Côté *et al*. reported a sensitivity of 71% for detecting such cases [24].

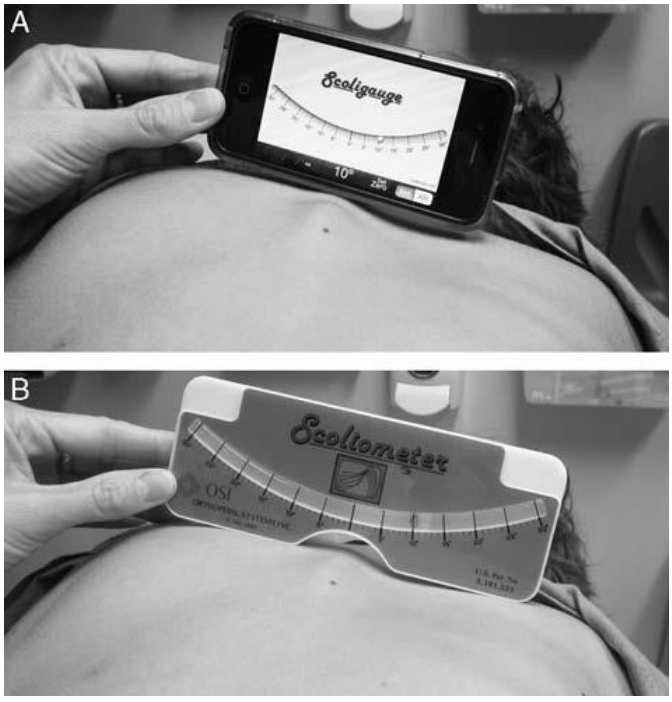


**Figure 5: (A) – Axial trunk rotation measurement with smartphone (B) - Measuremet with traditional Scoliometer, from [22]**

Whether or not the Scoliometer is ultimately beneficial to public health when used for scoliosis screening, it is not suitable for diagnosis, regular monitoring, or treatment assessment. Axial trunk rotation is correlated with vertebral rotation, which is in turn correlated with the Cobb angle [25]. However, the Cobb angle is a measure of the relative rotation of two vertebrae about an axis normal to the coronal plane. Despite

the correlation, this is an independent direction of rotation and distinct deformation. The Cobb angle must be measured accurately for diagnostic assessment and monitoring.

### 2.1.3 Optical

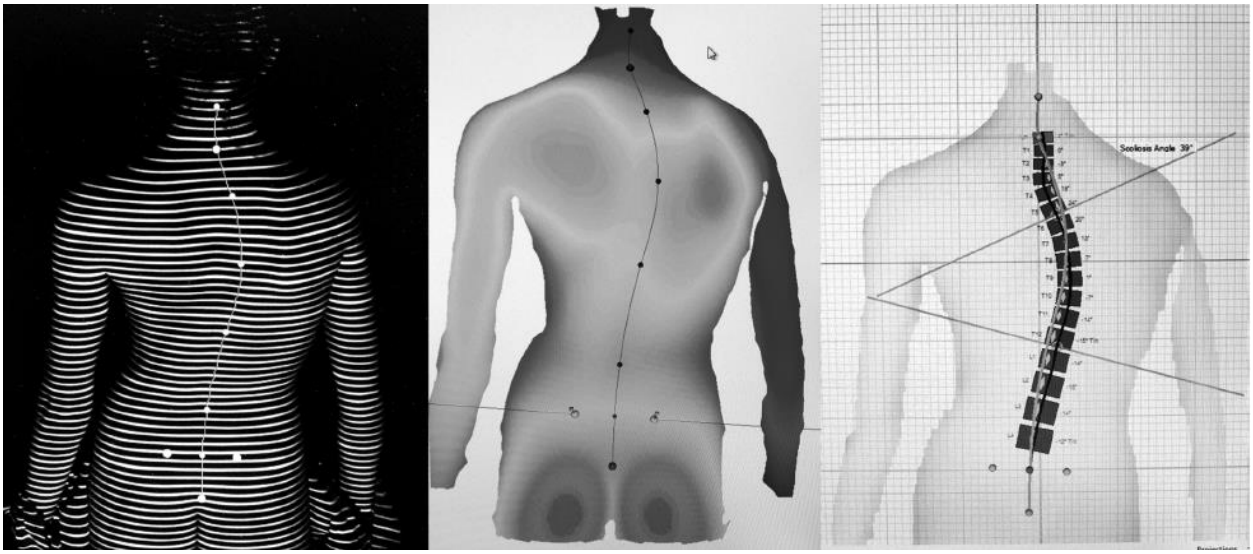


**Figure 6: (Left) - Structured light used to measure landmark locations shown as points. (Center) - Landmark based model and resulting topography (Right) - Skeletal model produced from landmark locations; all from [26]**

Optical methods are relatively new techniques under investigation for scoliosis assessment. They make use of light and vision systems to measure external asymmetry of a patient's back. Frerich *et al*. was able to measure multiple modes of spinal deformation by imaging structured light and constructing anatomic models with a Formetric 4D system [26]. Model assessment, performed by comparison with a database of thousands of model-radiograph pairs, even produces a geometric model of the spine at the vertebral level. Images from Frerich *et al*. in Figure 6 illustrate this structured light method and model generation.

Komeli *et al*. used multiple laser scanners to obtain a point-cloud representation of patients' backs [27]. The plane of best symmetry was found for the point cloud as the plane which minimizes the distance between points reflected across it to those originally across it. Torso asymmetry could then be assessed as the distance between each point and its reflected partner. This was then visualized as distance maps on

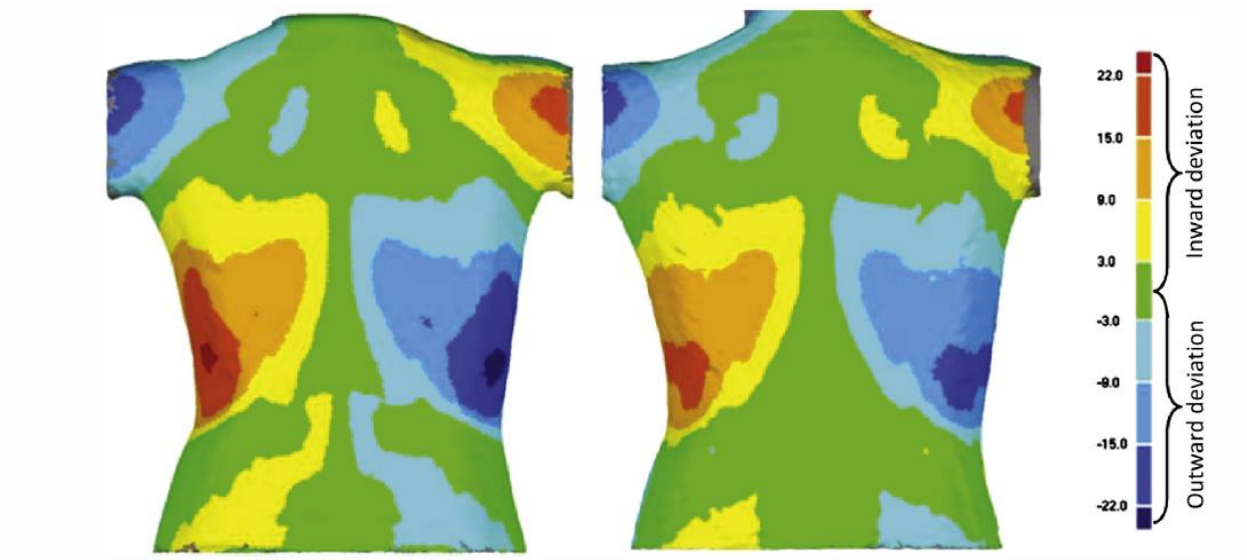


**Figure 7: Distance maps used to visualize torso surface asymmetry and classify deformation by Komeli *et al*. [27]**

projections of patients' backs, as shown in Figure 7. The aim of this study was mainly to investigate a novel classification method based on surface asymmetry. A subsequent work investigated the possibility of using features derived from surface measurement to identify whether patients' Cobb angles have progressed 5° or more as determined by X-ray [28]. Their classification trees used features including percent area changes in deviant surfaces, changes in maximum deviation, and changes in root-mean-squared deviation. Another study classified patients by their apical vertebra level and by curvature severity [29]. Again, X-ray was used to establish the ground-truth.

Despite the impressive inference of vertebral geometry from surface topography, external information is not suitable for diagnosis or routine assessment. Although measurement results were consistent across repeated tests with the Formetric system, lumbar and thoracic curves, thoracic kyphosis and lumbar lordosis were substantially and consistently under-predicted when compared with standard radiographic measurement [26]. Accurate measurement of these quantities, especially the larger of the thoracic or lumbar curves as the Cobb angle, is essential for the decision of whether or not to refer the patient for radiographic diagnosis. A method which under-predicted lumbar coronal curvature by nearly 10°, equal to the threshold for diagnosis, is not likely to be precise enough for public screening.

## 2.2 Diagnosis and assessment

Whether from a concerned parent or a positive screening result, suspicion of scoliosis is confirmed with radiographic assessment. The criterion for diagnosis is the measurement of a Cobb angle exceeding 10°. Once a child is diagnosed with scoliosis, they must return regularly for monitoring, to ensure that intervention can occur before the disease impacts their health. The Cobb angle is the gold-standard measure of scoliotic severity used for assessment in both monitoring and diagnosis. More advanced assessment generally uses CT or MRI to obtain a 3D model for the patient's spine. 3D visualization can be used to design an orthopedic brace, tailor physical therapy exercise, or to plan for surgery. The different imaging modalities commonly used for diagnosis and assessment of scoliosis are subsequently discussed in their respective sections.

### 2.2.1 X-ray

A posterior-anterior radiograph of the back will remain the standard assessment for scoliosis as long as the Cobb angle is the gold-standard for scoliosis quantification. This is not likely to change because of several favorable characteristics of radiography and the Cobb angle itself. The Cobb angle is a single measurement, performed on a single, planar image. Figure 8 shows a digitally rendered radiograph annotated with the Cobb angle and several other parameters of interest for scoliosis assessment.

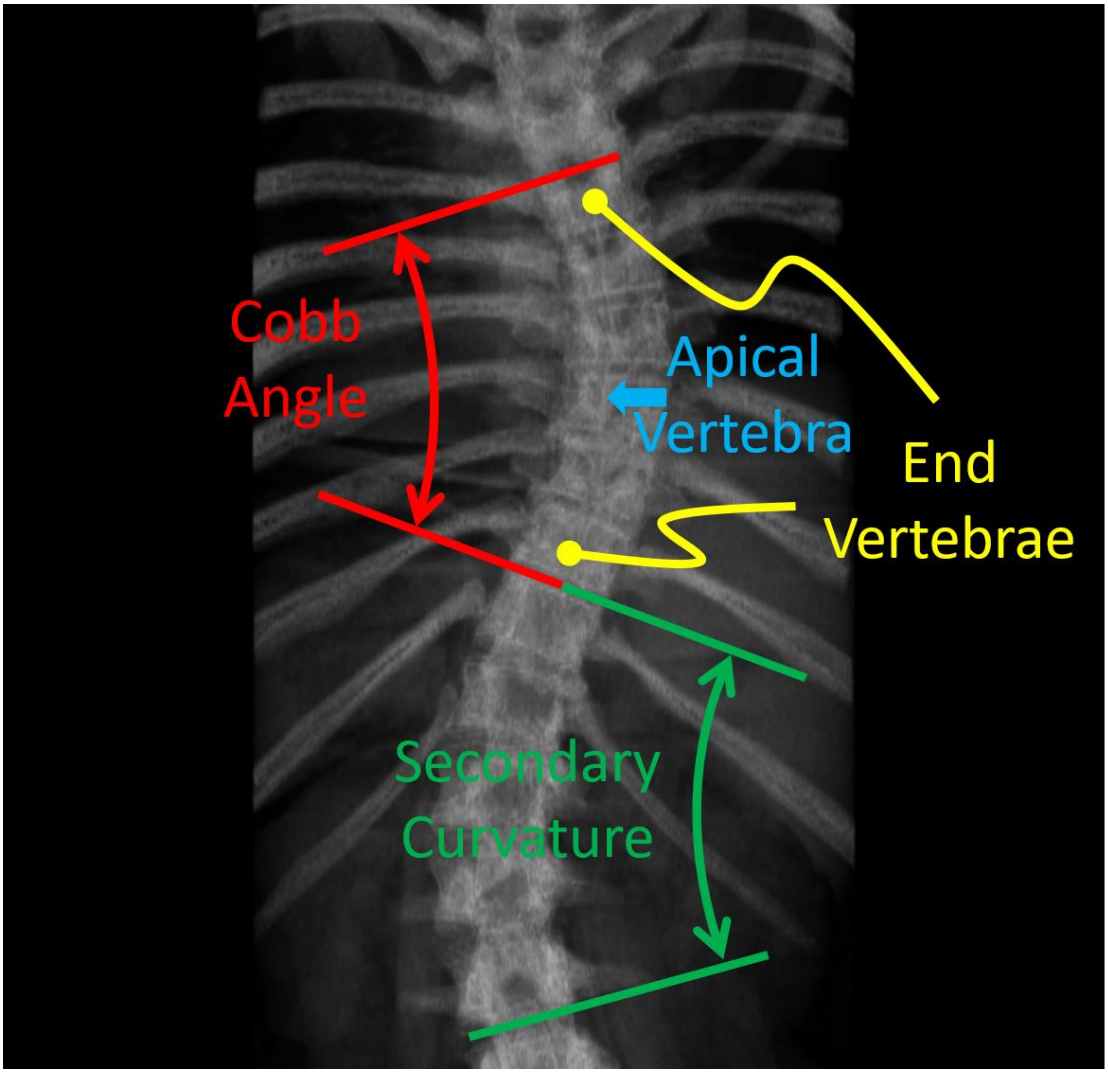


**Figure 8: DRR annotated with several parameters routinely examined in scoliosis assessment**

Defining the Cobb angle as the greatest angle between the endplates of any two vertebrae, projected onto the corona plane, was intended to minimize measurement variability. Nonetheless, any measurement is subject to variation. Tanure *et al.* lists mean errors in Cobb angle measurement from literature as ranging from 1.7° to 6.5°, and theirs as just over 3.5° [30]. Some of this error comes from variation in identifying the vertebrae that define the curve. Furthermore, vertebral endplates are never quite perpendicular to the image, and do not form unambiguous lines between vertebrae.

X-ray technology is ubiquitous; machines can be found at most clinics and hospitals worldwide. X-ray also produces good-quality images of the spine, in the sense that bone-tissue interfaces display high contrast,

and the full spine can be visualized in the imaging plane. Despite the utility of X-ray, its repetitive use during adolescence for scoliosis assessment is associated with an increased risk of cancer due to ionizing radiation exposure [31]. The dangers of radiation exposure, to both patients and practitioners, inflate the monetary cost of X-ray imaging, because of the need to comply with safety regulations.

EOS Imaging has developed a low radiation, biplanar X-ray system capable of 3D assessment of scoliosis in a standing posture [32]. This imaging system is referred to as EOS by EOS Imaging and in literature. Numerous investigations have been conducted regarding the economics of the EOS system for scoliosis assessment and there is generally agreement that the system is not economically viable [33]. Although the system provides a substantial reduction in ionizing radiation dose to the patient compared to conventional X-ray, the monetary savings to healthcare systems resulting from the corresponding reduction in cancer risks do not offset the high initial and operating costs of the system.

### 2.2.2 CT

CT imaging provides excellent 3D information about patient anatomy, including vertebral rotation and sagittal deformation. A segmentation of the spine from a CT scan produces the kind of visualization which practitioners can use to design braces [34], or make the decision to resort to surgical treatment. An example of a spine segmented from CT using a simple intensity threshold is shown in Figure 9.

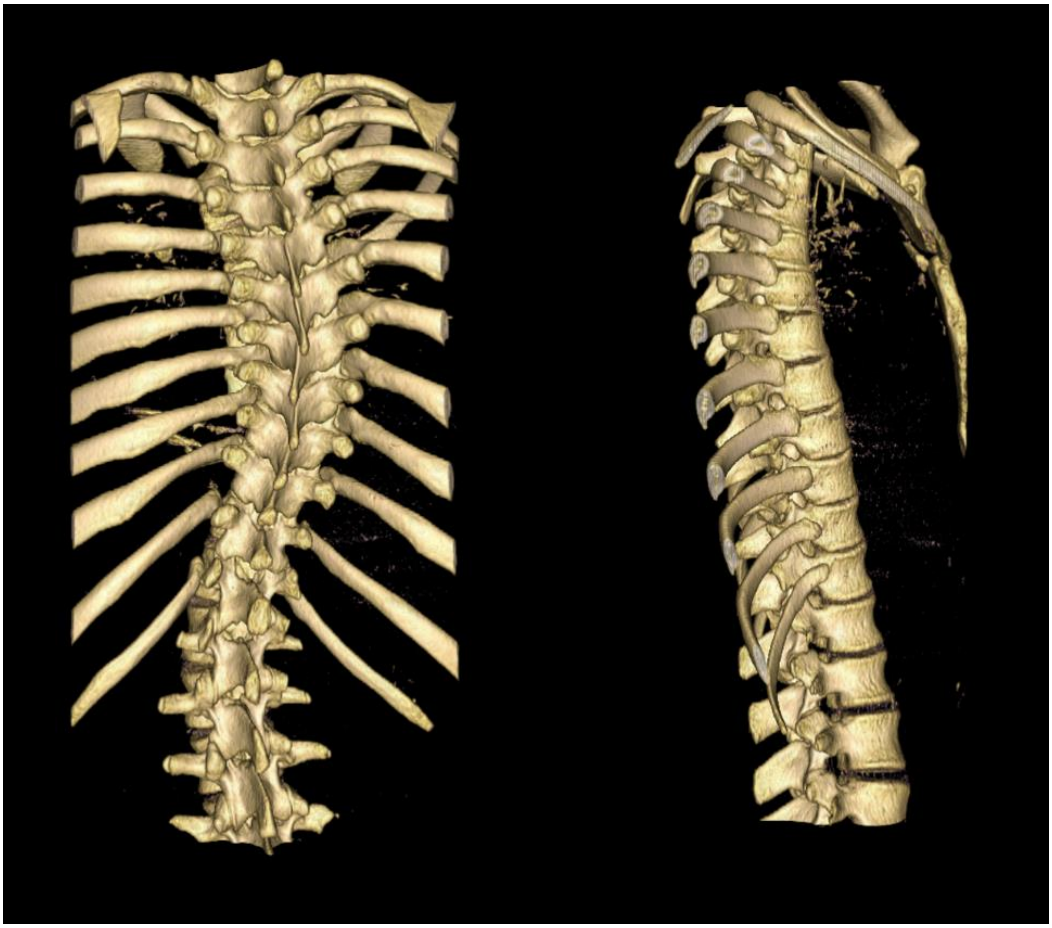

**Figure 9: Posterior and right views of torso CT segmented with an intensity threshold to show bones**

However, CT imaging has the same major drawback as regular X-ray radiography: the risks and costs associated with ionizing radiation. Furthermore, the availability of CT scanners is more limited than that of regular X-ray. Not only are CT scanners less common than X-ray machine, but scoliosis is assessed in a standing position, requiring special vertical scanners. These constraints make routine scoliosis assessment with CT risky in a hospital setting, and impossible in a chiropractic or physiotherapeutic setting.

### 2.2.3 MRI

MRI is a radiation-free alternative to X-ray and CT which is can produce high resolution, high contrast images of a patient's full spine. Schmitz *et al.* used MRI for 3D assessment of the effects of bracing on


**Figure 10: Projections of an axial MRI scan from the left-sagittal view, to right sagittal view, from [35]**

spinal deformation [35]. Projections of one of their scans is shown in Figure 10. Typical MRI machines, like the 1.5T Gyroscan ACS-NT PowerTrak 6000 system used by Schmitz *et al.*, scan patients in a supine position. However, scoliosis is assessed with the patient standing because the curvature increases when the spine bears weight. Diefenbach *et al.* used an upright MRI machine to measure Cobb angles and observed a good correlation with standard radiographic measurements, although they did not report measurement errors [36]. MRI is also particularly useful for imaging soft tissues which may be of interest in chiropractic treatment because of the information it may convey regarding back pain. Keenan *et al.* used MRI to measure vertebral wedging and disk deformation as these could provide information about how the scoliosis might progress [37]. Unfortunately, the availability of MRI machines constitutes a major drawback compared to X-ray. MRI machine are usually only available at large metropolitan or university hospitals. The availability of upright MRI machines, like that used by Diefenbach *et al.*, is even more limited.

## 2.3 Ultrasound-based assessment

### 2.3.1 Scoliosis assessment

Ultrasound-based assessment of scoliosis is a promising area of research. Ultrasound is a safe imaging modality as it has no known health risks. This implies relatively inexpensive safety standards which must be satisfied, compared with X-ray imaging. The inexpensiveness and safety of ultrasound have contributed

to its proliferation in clinical and research applications. The tradeoff for the economy and portability of ultrasound is the limited field of view and low image quality, compared to other modalities. There is essentially no difference between a single 2D spinal ultrasound image of a scoliotic and healthy patient. Therefore, a series of ultrasound images, on their own, are not suitable for scoliosis assessment. They can only provide small planar parasagittal and axial views of anatomic landmarks. Scoliotic deformity, however, is characterized by the overall shape of the spine, by the geometric relations between these anatomic landmarks. Therefore, ultrasound-based scoliosis assessment employs spatial tracking. An electromagnetic or optical position tracker fixed to the ultrasound probe, with one fixed to the patient for reference, provides position information for each image captured.

Spatially tracked ultrasound has been used in numerous ways for scoliosis assessment. Purnama *et al.* demonstrated a method for using optically tracked ultrasound images to construct a 3D volume from which various skeletal landmarks could be located [38]. Chen *et al.* used a mechanically positioned ultrasound probe to obtain images with spatial information [39]. They used maximum intensity projection to create coronal images of the phantoms' and patients' complete thoracic and lumbar spines. The centers of the laminae were identified in these coronal images and used as landmarks to measure the tilt of the vertebrae. The angle between the two most mutually tilted vertebrae served as an approximation to the Cobb angle. Figure 11 shows this measurement both on a patient's X-ray and on one of the coronal images constructed from ultrasound. Ungi *et al.* used an electromagnetically tracked

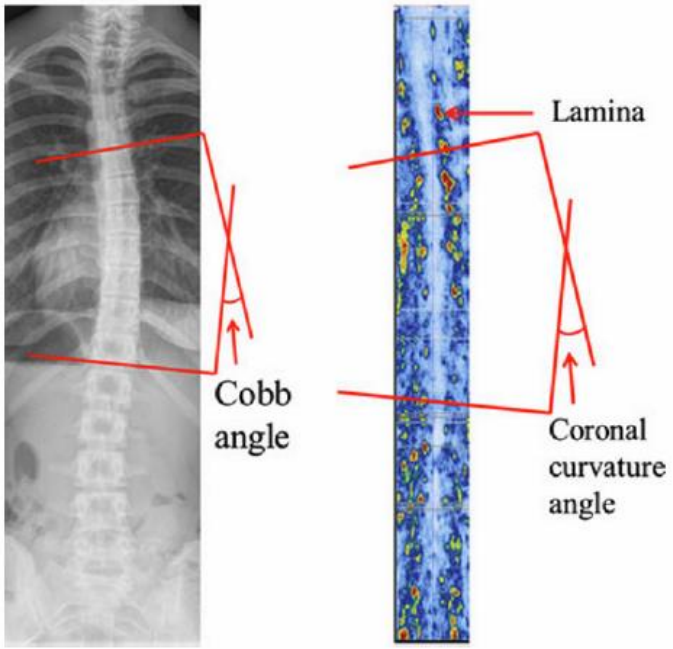


**Figure 11: Comparison of standard radiographic Cobb method with center of laminae method from [39]**

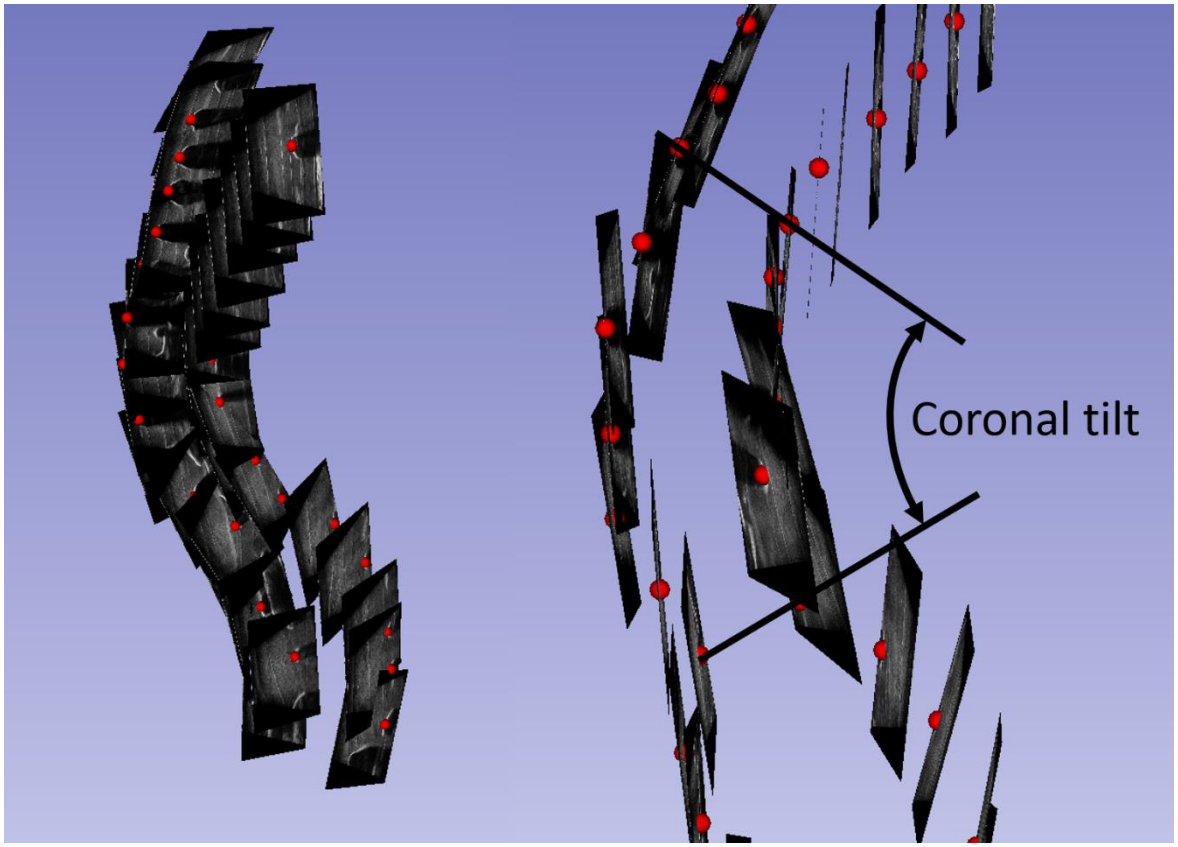


**Figure 12: (Left) - Ultrasound snapshots of scoliotic spine in 3D space; manually identified transverse process locations shown as red points (Right) - Characterization of scoliotic severity with angle between maximally tilted vertebrae by landmarks as used by [40]**

ultrasound probe to identify transverse processes from their characteristic response in a parasagittal orientation [40]. Rather than perform a complete scan for subsequent volume reconstruction, ultrasound snapshots were captured where they depicted transverse processes. After loading the snapshots into a 3D environment, the transverse processes were manually located and used as a proxy to the Cobb angle via the vertebral tilt. Figure 12 shows such a set of ultrasound snapshots in 3D space with markers placed on the transverse process locations, and the use of those landmarks to obtain the angle of coronal tilt.

Cheung *et al.* [41] and Wang *et al.* [42] both used spatially tracked freehand ultrasound probes to render 3D models of the spine similarly to Chen *et al*. Cheung *et al*. used these models to locate the transverse processes and superior articular processes while Wang *et al.* used the laminae. Assessment based on these landmarks also used vertebral tilt as a proxy to the Cobb angle. Both methods used special ultrasound

transducers, wide enough to image the entire width of the spine simultaneously. They also used different support frames to position the patient. Cheung *et al*. performed the assessments with the patients standing against a chest board, while Wang *et al.* used a couch with a slot cut out for supine assessments.

Nguyen *et al.* predicted Cobb angles to within 5° in phantom and pilot clinical tests [43]. They measured vertebral tilt as well as axial rotation from a model composed of surfaces. The surfaces were generated from a collection of points, approximately 20 points per ultrasound image. The points were located manually by operators, with assistance from spline interpolation. Each image took roughly 15s of processing according to the authors. To save time, typically 170 of the ultrasound images were used to generate points out of the 850 images captured. Still each scan required an hour of manual processing. Nguyen *et al.* produced visually impressive representations of the spine, if at the expense of extensive user input. Other groups have explored the problem of automatically detecting bone surfaces in ultrasound images.

### 2.3.2 Bone segmentation

The methods discussed above demonstrate that performing patient-specific scoliosis assessment requires identification of skeletal landmarks in ultrasound images. Ultrasound images in general are difficult to interpret because of their high signal-to-noise ratio, imaging artifacts, and the orientation and small size of the image plane. Furthermore, a single ultrasound scan can consist of many images. Manually identifying bony features is impossibly burdensome in a scan of the entire spine, consisting of hundreds or thousands of images. Snapshot and rendered model methods make manual identification of skeletal landmarks more convenient but still time consuming and unreliable. Manually identifying a series of landmarks along the spine will inevitably be slower than X-ray to assess coronal curvature as X-ray can image the coronal plane immediately.

To the ends of improving patient assessment accuracy, reducing operator workload, and reducing intra and inter-operator variability, research efforts have investigated automatic segmentation of bone in ultrasound. The nature of ultrasound images, and the responses produced by bones in them make this a challenging

problem. Characteristics of bone in ultrasound are discussed below, before reviewing some methods which have been investigated to automatically segment them.

The large difference in acoustic impedance between soft tissue and the bone beneath it is a characteristic of bone which can serve to both identify and conceal the bone. The high impedance of bone can cause nearly all of the acoustic energy to be reflected back to the transducer, producing two effects characteristic of bone in ultrasound. First, with so much energy being reflected at once from the bone surface, a bright line appears in the ultrasound image. Second, with so little energy continuing past this surface, a dark acoustic shadow is seen below the bone. These characteristic responses of bone in ultrasound are clearly visible in Figure 13. This bright surface response can only occur when the angle between the bone's surface normal and direction of propagation of the acoustic beam is small. As this angle increases, two

**Figure 13: Parasagittal ultrasound image of a phantom model's transverse processes**

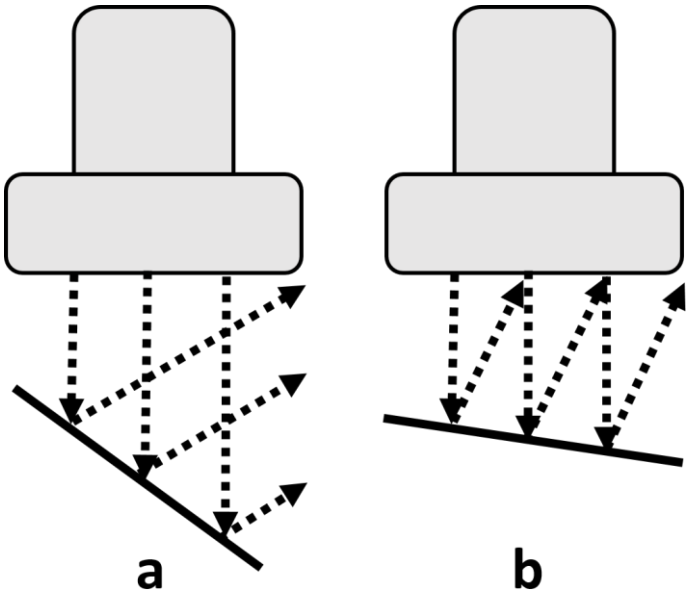


**Figure 14: (a) - Bone surface steeply inclined relative to probe reflects signal away (b) - Mildly inclined bone surface can reflect signal to different spots on transducer**

phenomena, common in cause but opposite in result, can occur. First, the bone surface can reflect the acoustic energy away from the transducer, eliminating the bright surface response. Second, the surface can reflect the energy towards another piezoelectric crystal in the transducer. The bone-like response observed at another location on the probe, delayed relative to a nearby flat surface, gives the bone an apparent thickness in ultrasound. These phenomena are illustrated in Figure 14.

Numerous methods have been proposed to automatically segment bone from B-mode ultrasound images, building on basic image processing techniques [44]. Foroughi *et al.* used known characteristics of bone in ultrasound to design a segmentation method [45]. They used dynamic programming to extend contours along bright surfaces, normal to the ultrasound waves, with dark shadows beneath them. Different methods have employed variations of image thresholding to recognize the bright response which bone surfaces produce in ultrasound. Kowal *et al.* augmented a basic threshold with depth-weighting as a geometric heuristic to preferentially recognize deeper bright structures as bone [46]. Masson-Sibut *et al.* employed a vertical gradient operation before thresholding, since bone surfaces are likely to be visible when they face the direction of ultrasound propagation, and produce a marked change in brightness compared to soft tissue above and acoustic shadow below the surface [47].

Most methods use some kind of morphology, both to eliminate small groups of false-positive pixels and to consolidate correctly segmented pixels of a given bone surface. Kowal *et al.* used a 'pixel cloud stock exchange' where pixels identified as belonging to a cloud were assigned particular values based on their positions in the image and relative to other pixels [46]. This value reflected the likelihood that a pixel was bone. It increased with the number of pixels in the cloud and decreased close to the probe. Pixels would use this value to buy other pixel groups into their own, consolidating a bone surface. Masson-Sibut *et al.* used island removal to eliminate false positive pixels, pixels groups smaller than 5 pixels where pixels belonged to a given group if they were within a 3×3 neighborhood of one another [47].

Hacihaliloglu *et al.* proposed the use of phase information in ultrasound images as a means of identifying bone surfaces [48] [49]. Phase-based methods generally make use of banks of quadrature band-pass filters

which respond to local structural symmetry. Filters are chosen and tuned to identify the symmetry and orientations expected from the ridges which bone surfaces produce in B-mode ultrasound images along the scanlines. In a different application than the spine, Abu Anas *et al.* combined phase symmetry with acoustic shadow measurement from Foroughi *et al.* to segment the surface of the scaphoid in ultrasound [50]. They then used point clouds derived from the segmentation to register a statistical scaphoid model to phantom ultrasound data. Their method was more computationally expensive than [48] or [49], but particularly suited for identifying blurred bone surfaces.

Machine learning has also been investigated as a tool to segment bone in ultrasound. Berton *et al.* trained a linear discriminant analysis classifier to identify different structures in axial spinal ultrasound [51]. Individual pixels were ascribed to one of three groups: spinous process, acoustic shadow, or other tissue. Classification was performed based on features like the bone probability map from Foroughi *et al.*, local phase symmetry from [48], and image gradients from a Sobel edge detector. Classification was generally good, achieving roughly 90% classification accuracy for each pixel group. However, of 175 ultrasounds, only 107 were deemed to be of sufficient quality for the study.

A segmentation of the bone surfaces from a spinal ultrasound scan, by itself, provides a 3D representation of a limited portion of the spine. Bone surfaces normal to the direction of ultrasound are those that can be seen and segmented. These visible bone surfaces may be used to derive landmarks to estimate scoliotic curvature, but do not provide a 3D visualization of patient specific spinal anatomy at the vertebral level, like a CT or MRI segmentation.

### 2.3.3 3D visualization

The angle of coronal curvature, whether measured from X-ray or one of the ultrasound-based methods, is useful information for making decisions regarding when to begin treatment. A physiotherapist or chiropractor, who may be limited to ultrasound imaging, may still wish to obtain 3D visualizations of patients' vertebral anatomy. Such a visualization could demonstrate the progression of a scoliotic curve to an adolescent patient or their parents, where a series of numerical angles or even the models used in the

ultrasound based assessment methods may not. The ultrasound-based scoliosis assessment methods described above are useful as alternatives to X-ray for coronal curvature measurement, but are not intended to produce 3D vertebral visualizations. Several methods have been developed producing 3D visualizations of spinal anatomy at the vertebral level, though none suitable for the purpose of purely ultrasound based scoliosis assessment, as we will see.

Rasoulian *et al.* produced 3D spine visualizations for injection navigation by registering a statistical spinal atlas to a tracked ultrasound scan. The statistical atlas was generated from the CTs of 32 patients' lumbar spines, and parameterized the shapes and poses of the vertebrae. Initial *in vivo* results indicated that the facet joints could be identified to within roughly 5mm when compared with CT ground-truth. The feasibility of generating patient-specific spinal visualizations suitable for interventional navigation using only ultrasound imaging is an exciting prospect. Unfortunately, the derivation of a statistical atlas suitable for scoliosis assessment presents additional challenges. The variability in the shapes and poses of even healthy vertebrae require multiple samples to estimate; Rasoulian *et al.* used 32 CT scans. Scoliosis presents with far more variability in vertebral shapes and poses than healthy spines. A data set with enough samples to capture each mode of deformation possible in scoliosis, at each possible location in the thoracic and lumbar regions, remains to be developed.

## 2.4 Summary

Scoliosis is a disease characterized by spinal deformation that can affect people of all ages. The most common variety of the disease is adolescent idiopathic scoliosis. Detection typically occurs when asymmetry is noticed in the torso. Although public screening programs may improve detection rates, there is some controversy regarding the overall utility of such programs. A patient is definitively diagnosed with scoliosis when the Cobb angle measurement from an X-ray exceeds 10°. Once diagnosed, the progressive nature of the disease requires that the patient return every few months for reassessment, to monitor curvature progression. X-ray remains the gold-standard for both diagnostic and regular monitoring assessment, though 3D assessment such as CT or MRI may be performed for treatment planning.

Research in ultrasound-based scoliosis assessment has shown promise in addressing a number of issues. Most notably, ultrasound does not employ ionizing radiation, thereby reducing health risks compared to routine X-ray. It is also a more accessible technology than CT or MRI. When combined with spatial tracking, ultrasound images can be used to perform 3D assessment of the patient's anatomy. Various parameters characterizing deformation can be computed from landmarks located with 3D ultrasound. Segmentation methods have been used to automatically identify bone in ultrasound, usually for skeletal model registration. There remains a need for a method which can produce complete spinal visualizations suitable for 3D scoliosis assessment, which makes use only of ultrasound imaging.

# Chapter 3

# 3D visualization of scoliotic spine with ultrasound

The work presented in this chapter has recently been adapted and incorporated into work by Baum *et al.* [52]. Specifically, the method for warping a healthy-shaped model to patient landmarks collected from ultrasound is used. Baum *et al.* adapted the method so that the visualization is generated while the operator is performing the tracked ultrasound scan, once several landmarks have been manually identified. This initial visualization is meant to help the operator locate subsequent landmarks. Subsequent landmarks are then used to update the visualization and the process repeats. Baum *et al.* found that operators generally liked the visualization-assisted landmark location method in that it helped them locate the landmarks and was easy to learn and use.

## 3.1 Overview

The method presented in this chapter, first descried in Church *et al.* constitutes a key contribution of this thesis [1]. It describes how transverse process locations can be used to constrain the registration of a healthy spine model to patient anatomy. This addresses the need for a method which uses ultrasound data, the transverse process locations, to generate spinal visualizations capable of depicting patient-specific scoliotic deformity. The method consists of:

i. Locating the patient's transverse processes to serve as anatomic landmarks
ii. Supplementing these landmarks with anchor points
iii. Using the natural landmarks with the anchor points to constrain a thin-plate spline registration
iv. Using the thin-plate spline to deform the healthy-shaped model to the patient's anatomy

The method is validated by comparing the deformed model to a ground-truth surface derived from patient CTs. An overview of this method is shown in flowchart form in Figure 15. The following sections then describe the derivation of the data used by the method, the healthy-shaped model and the transverse process

landmarks. Subsequent sections describe the registration and warping used to produce the visualization, then validation of the method, and discussion.

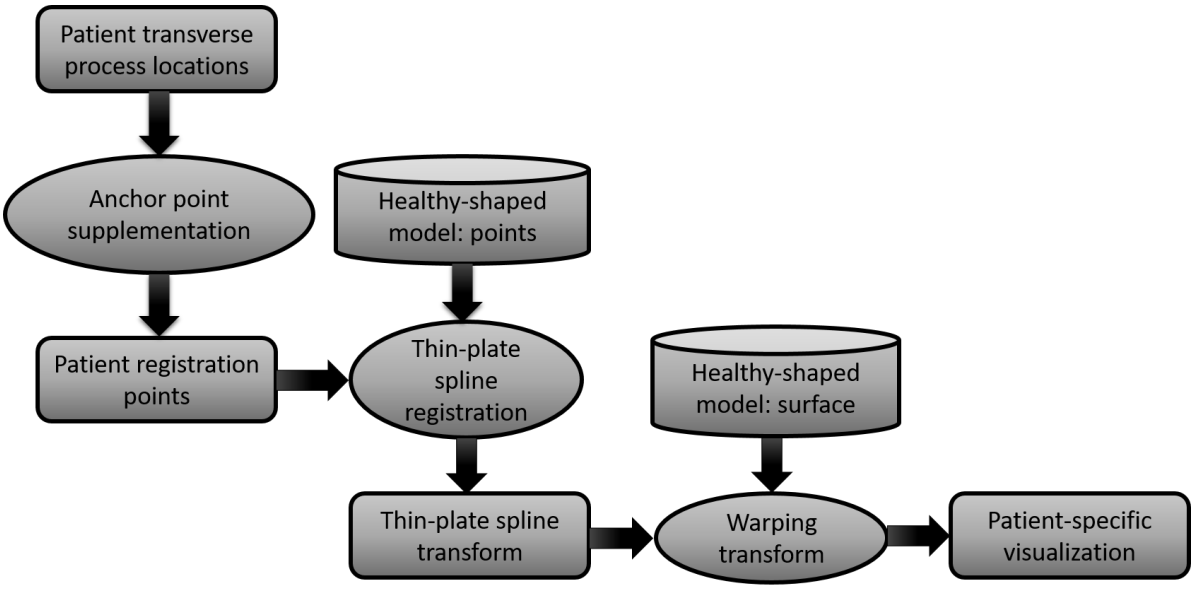


**Figure 15: Proposed method for patient-specific spine visualization from ultrasound-accessible transverse process locations. Rectangles represent patient-specific data, ovals represent processes. Healthy-shaped model data is represented with cylinders to indicate persistence.**

### 3.2 Healthy-shaped model

The main idea of this visualization method is to deform a healthy-shaped spine model to patient anatomy. The healthy-shape model used in this method was segmented from a cadaver's CT scan and can be found at [53]. The healthy-shaped spine is represented as a closed-surface model. That is, a collection of vertices and edges which can be rendered as a geometric surface in a virtual 3D environment. It was truncated to contain only the thoracic and lumbar vertebrae, as these are the regions primarily affected by scoliosis and consistently present in the available scans. The vertebrae were then segmented individually from one another and the vertebral disks, allowing for the creation of healthy-models corresponding to whatever length of the patient's spine is scanned. Since the visualization method uses the transverse process locations for landmark-based registration to deform this model, points were manually placed on these landmarks. This healthy-shaped model and manually identified landmarks are shown in Figure 16.

### 3.3 Transverse process landmarks

The transverse processes, shown with other vertebral anatomy in Figure 2 and marked in Figure 16, were chosen to be used as landmarks for healthy-model to patient registration. The design of this method with ultrasound in mind lead to this choice. The transverse processes are likely the easiest landmarks to locate with ultrasound. Their particular geometry, that is, their lateral protrusion from other vertebral anatomy and the boneless spaces between transverse processes of subsequent vertebrae produce an easily recognizable characteristic response in parasagittal ultrasound. A parasagittal ultrasound is compared to an axial one in Figure 17. The left image depicts transverse process surfaces, regularly repeating along the spine. The right image demonstrates the characteristic 'bat shape' of the posterior vertebral surface in an axial ultrasound image. In the axial image, the spinous process, articular and transverse processes, laminae and anterior surface of the vertebral body are all visible.

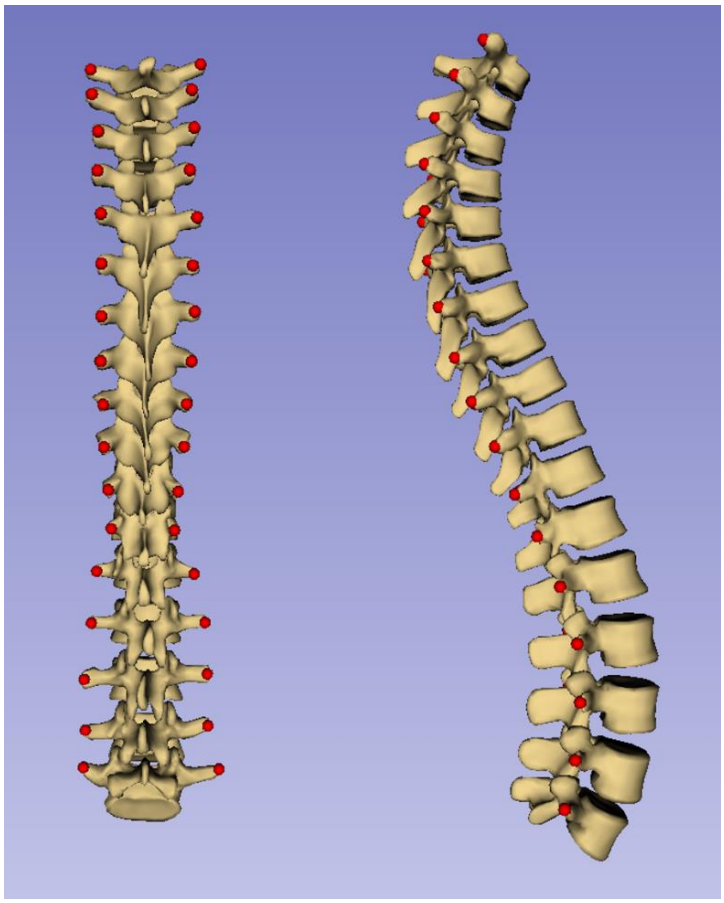

**Figure 16: Healthy-shaped spine model with transverse process landmarks as red points**

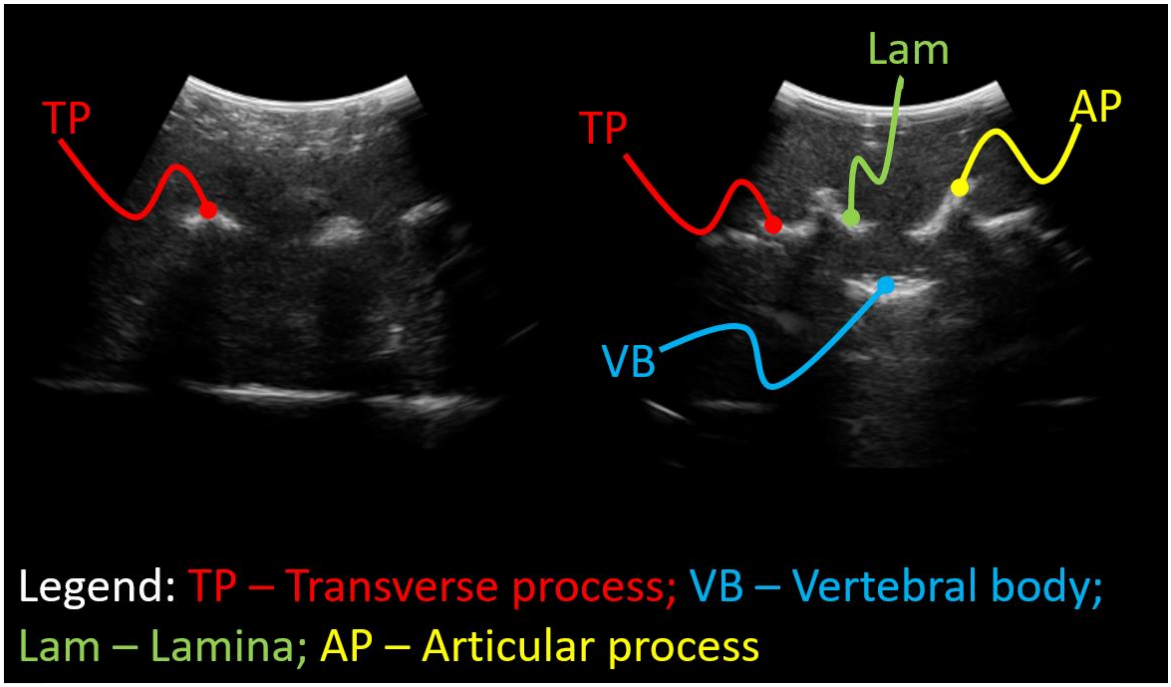


**Figure 17: (Left) - Parasagittal spinal ultrasound (Right) - Axial spinal ultrasound;**

Ultrasound-based scoliosis assessment methods, like Chen *et al.* [39] or Cheung *et al.* [41], used scans to render models from which skeletal landmarks were located. Curvature measurements were extracted from these landmarks. Our proposed visualization method uses such skeletal landmarks as input. Visualization could immediately be generated as a supplement to these ultrasound-based curvature assessment methods. In fact, rendering of a model prior to our visualization is unnecessary. The curvature quantification method of Ungi *et al.* [40] recognized that landmark locations captured with tracked ultrasound snapshots are

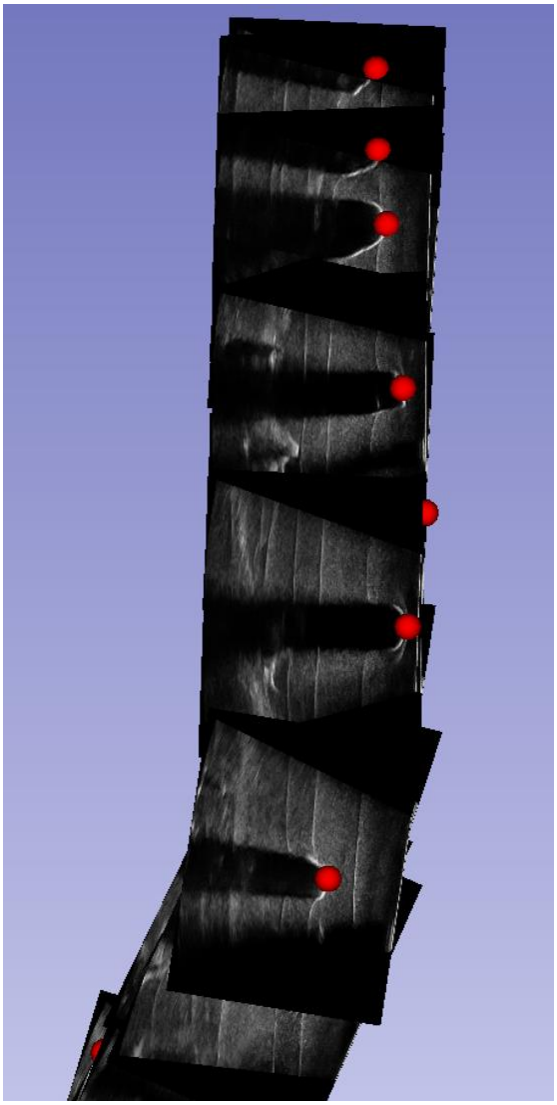

**Figure 18: Side view of tracked parasagittal ultrasound snapshots depicting transverse process responses**

enough to quantify spinal curvature, provided that exact landmark points can be placed accurately on the snapshots. Figure 18 shows the same ultrasound snapshots as Figure 12, but from a side view. The transverse processes are simpler to image in a parasagittal orientation, so a snapshot can more easily be capture with the landmarks in better view than in an axial orientation. The simpler images then reduce variability in manual landmark identification. The ultrasound images in Figure 17 and Figure 18, are only to illustrate characteristics of the transverse process in ultrasound. These particular landmarks were not used in this study.

The transverse processes used to generate the results for validation of this visualization method were collected from CT segmentations for two reasons. First, these scoliotic patients underwent CT scans as part of pre-interventional assessment; tracked ultrasound scans were not collected in association with the CTs. The second reason is that landmarks accurately located from CT allow more general validation of the visualization method. The method can be validated using ideal data, accurately located landmarks, or using data with known error statistics. Furthermore, Chapter 4 is devoted to making landmark sets with missing points or other defects suitable for this visualization method.

## 3.4 Thin-plate spline landmark registration

A landmark-based thin-plate spline registration was chosen as the method for warping the healthy-shaped model into patient anatomy. The thin-plate spline has long been used for a smooth interpolation of 3D points [54] and several reasons make it a natural choice for this registration.

### 3.4.1 Thin-plate spline

A thin-plate spline registration uses deforming transformations to warp surfaces or bodies, modelling deformations in those bodies. This is done by transforming the locations of source landmarks to match corresponding target landmarks, and interpolating the transforms. In this manner, transforms are computed for each point in the source coordinate frame. This is rather different than a rigid registration algorithm which computes a single transform for the entire coordinate frame, preserving distances within the source points while minimizing their collective distance to the target points. The registration first instantiates transforms describing how to move each source landmark onto its corresponding target landmark. In this case, source is the healthy-shaped spine model, the target is the patient, and the landmarks are their transverse processes. These transforms can be represented as matrices, and their translation components can be visualized as arrows, as in Figure 19.

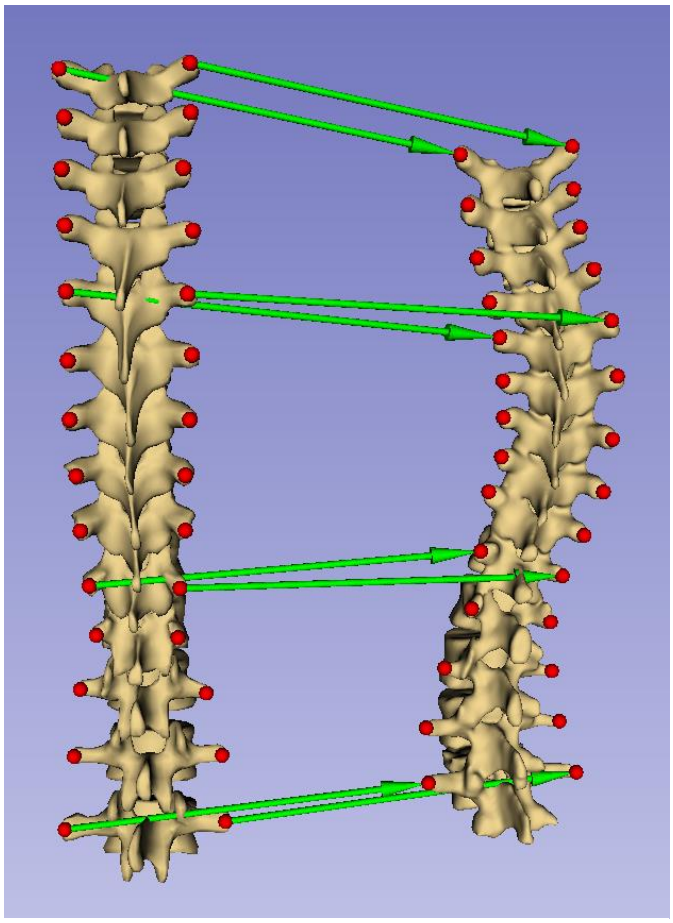

**Figure 19: Thin-plate spline gives each source landmark transform to corresponding target landmark**

The next step in registration is interpolation of the landmarks' transforms. The thin metal plate is the model used to produce realistic semi-rigid

or plastic deformation in the source coordinate frame. The energy function used to determine the interpolated transforms' values is derived from the energy needed to deform a thin plate of metal. As in a thin plate of metal, the energy required to deform it is related not only to in-plane tension or compression, but to curvature bent into the sheet. The particular transform values chosen are those which minimize the deformation energy of the coordinate frame upon registration. This can be visualized as the deformation of a wire grid, as in Figure 20. The undeformed grid on the left of Figure 20 shows the coordinate frame without deformation, where the identity transform is associated with each point in the frame. The mesh on the right shows how thin-plate spline interpolation of transforms between landmarks produces physically realistic deformation throughout the coordinate frame.

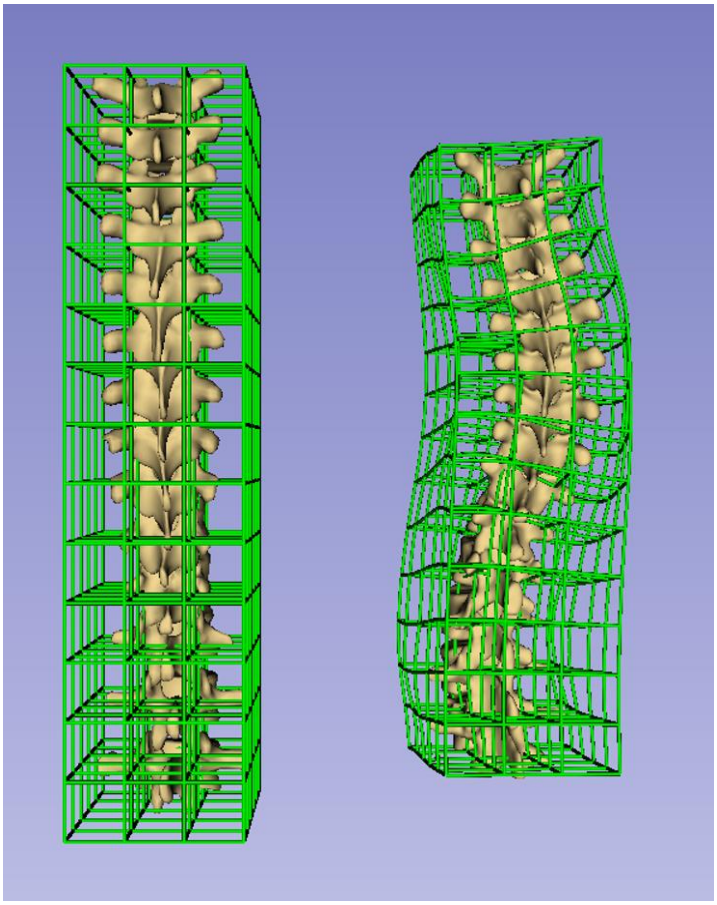

**Figure 20: (Left) – Undeformed coordinate frame around healthy-shaped spine model (Right) – Coordinate frame deformed to patient anatomy with thin-plate spline registration**

Certain aspects of the spline, including but not only its physically-inspired energy function, make it suitable for realistically deforming a healthy-shaped spine to visualize scoliotic anatomy. Both spines and splines are composed of repeating units; for each vertebra in the spine, the spline has a polynomial segment. In this case, it is a polynomially interpolated combination of affine transformation which minimize the energy function of the coordinate frame deformation. The dependence of the energy function on curvature prevents

anatomically unrealistic deformations from being produced. Anatomically realistic deformations of the spine exhibit small curvatures at small scales; neighboring vertebrae are physically constrained by muscles, ligaments, and intervertebral disks to be similarly oriented. The curvature of the spline is measured by its radius at each point in the coordinate frame. Therefore, it can accommodate large global deformation in a large structure, like a scoliotic spine with a Cobb angle exceeding 90°.

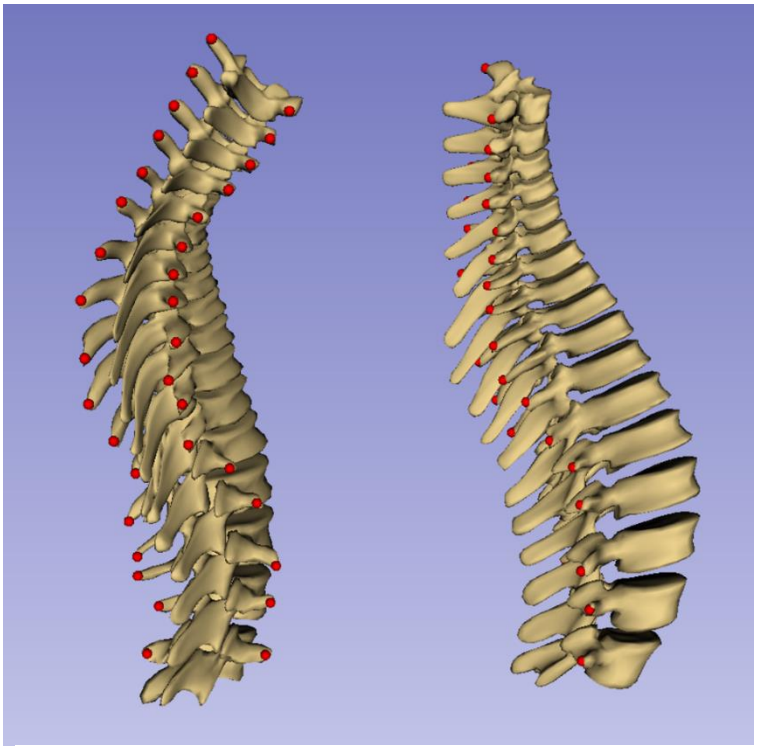

**Figure 21: Surface visualization resulting from thin-plate spline registration between only the patient and healthy-shaped model's transverse process landmarks**

### 3.4.2 Anchor point supplementation

The transverse process locations by themselves, although suitable for measurement of scoliotic curvature, do not provide sufficient constraint to the 3D thin-plate spline. This is because of the particular distribution of the transverse processes. They have an axial distribution along the spine, with two landmarks at each vertebral level, and a lateral distribution across the spine due to bilateral symmetry. The landmarks little distribution normal to these two directions, as they lie along the posterior surface of the spine. The thin-plate spline registration cannot accurately interpolate transforms normal to the direction of this surface because interpolation requires a distribution. The results of using only the transverse process landmarks for the thin-plate spline registration are visualizations like the one shown in Figure 21.

The proposed solution is to compute the direction lacking constraint from the existing transverse process landmark distributions, and add anchor points in that direction. One anchor point was added to each transverse process location. The direction in which the anchor point was offset from its transverse process

was computed as the cross-product of a lateral vector between landmarks of a given vertebra, and an axial vector between landmarks at different vertebral levels. This process is subsequently described in mathematical detail, and then exemplified in Figure 22.

To compute *P*(i, j),* the location of the anchor point corresponding to natural landmark at *P(i, j),* where *i* denotes the vertebral index (superior-most being *i = 0*) and *j* denoting left versus right (*j = 0* for left, *j = 1* for right), an offset vector indicating the anchor point's location relative to the natural landmark was computed. The offset vector was the cross product of a lateral vector between landmarks of a given vertebrae, and an axial vector between landmarks of neighboring vertebrae, where the lateral vector was computed as:

$$\langle Lat(i,j)\rangle = \langle P(i,j)\rangle - \langle P\big(i,(j+1)(mod\ 2)\big)\rangle \quad (1)$$

where angled brackets denote vectors. The formulation for the lateral vector allows for them to point from right to left, or vice versa. When cross-produced with axial vectors consistently pointing from the superior to inferior directions, this would result in different anchor point offset vectors pointing in opposite directions. To ensure anchor points were consistently placed towards the vertebral bodies from their natural landmarks, any offset vector with a negative anterior-posterior component was reflected by multiplying each component by *-1*.

The superior-inferior vector was computed as the average of two possible vectors:

$$\langle Ax(i,j)\rangle = avg[\langle P(i+1,j)\rangle - \langle P(i,j)\rangle, \langle P(i,j)\rangle - \langle P(i-1,j)\rangle] \quad (2)$$

Superior and inferior ends of the spine constituted boundary conditions where only one of these two possible vectors were available. In these cases, only this available vector was used. Finally, to determine the location of the anchor point, the offset direction was computed as the cross-produce of the lateral and axial vectors, normal to both of them. The magnitude of the normal vector is determined by an anatomic scaling factor:

$$\langle P^*(i,j)\rangle = \langle P(i,j)\rangle + \langle Norm(i,j)\rangle = \langle P(i,j)\rangle + ASF \cdot unit[\langle Lat(i,j)\rangle \times \langle Ax(i,j)\rangle] \quad (3)$$

where * denotes the anchor point being added, *ASF* is a patient specific anatomic scaling factor, • denotes scalar multiplication, × denotes a vector cross-product, and *unit[V]* is the unit vector in the direction of vector *V*.

The anatomic scaling factor is meant to convey the difference in length-scale between the healthy-shaped model and individual patient's anatomy in the distance between the transverse processes and their corresponding anchor points. It was simply the overall length of the spine, averaged over both sides and over the number of vertebrae present:

$$ASF = \frac{\sum_{i=0}^{N-1}\sum_{j=0}^{1}|\langle P(i,j)\rangle - \langle P(i+1,j)\rangle|}{2 \cdot N} \quad (4)$$

where *N* is the number of vertebrae and |*V*| is the length of vector *V*.

Figure 22 is illustrated with 3 vectors. It shows the green normal offset vector at the 8th thoracic vertebra, computed from the blue axial vector and the yellow lateral vector. This exemplifies the determination of the direction to offset the left anchor point for this vertebra, *P*(8,0)*, from its corresponding transverse process landmark, *P(8,0)*. The vector illustrations are inexact as the glyphs were added after anchor point supplementation for illustration purposes, not rendered from computation.

Once the manually located, natural transverse process landmarks are algorithmically supplemented with anchor points, the thin-plate spline registration is performed. This quantifies differences between patient and healthy model landmarks as transforms though space, deforming a coordinate frame. Patient-specific visualizations are generated by placing the healthy-shaped surface model in the deformed coordinate frame. This warps the healthy-shaped surface model to the patient's ultrasound data to generate a surface visualization of the patient's spine.

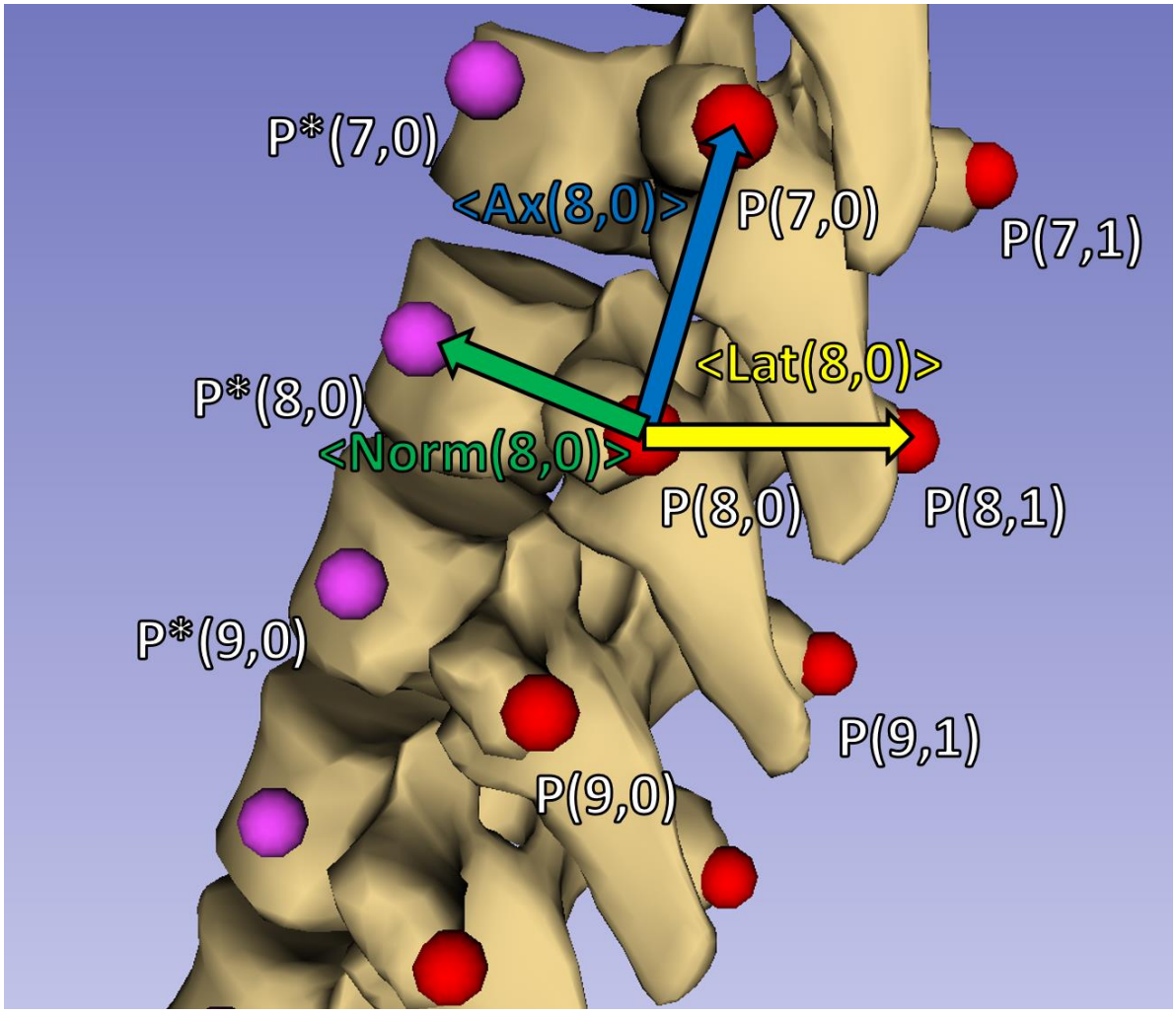


**Figure 22: Illustration of vectors used to derive anchor point locations (purple) from transverse process locations (red)**

### 3.5 Results and discussion

To validate this visualization method, the visualizations generated from transverse process locations were compared to spine surfaces manually segmented from CT scans. Manually segmenting a patient's entire vertebral anatomy from a CT scan usually took 2-3 hours. Limited time allowed for segmentation of 16 patients' CTs. The fact that these patients have not had tracked ultrasound scans associated with their CTs precluded the possibility of testing this method with landmarks located from ultrasound. Instead, their transverse processes were manually located manually from these CT-derived ground-truths. This allowed validation of not only the method's ideal performance, using accurate landmark locations, but also

validation of its performance using landmarks with known error statistics. Testing the method using landmarks with simulated errors provides some indication of how the method may perform if landmark locations are more variable when derived from ultrasound.

Validation metrics were computed from results using four landmark sets. The first set, manually located from the CT ground-truths was used to derive the other three. Three landmark sets were created by adding random noise to landmark locations with standard deviations of $1mm^2$, $3mm^2$, and $5mm^2$, respectively. Average and maximum Hausdorff distances, and Dice coefficients were computed to quantify the accuracy of the registrations. Table 1 shows the Hausdorff distances and Dice coefficients for the visualizations to ground-truth models, for each amount of landmark noise.

**Table 1: Registration metrics for each patient, for each amount of landmark location noise**

| | | Maximum Hausdorff distance (mm) | | | | Average Hausdorff distance (mm) | | | | Dice coefficient | | | |
|---|---|---|---|---|---|---|---|---|---|---|---|---|---|
| **Patient #** | **Noise ($mm^2$)** | **0.0** | **1.0** | **3.0** | **5.0** | **0.0** | **1.0** | **3.0** | **5.0** | **0.0** | **1.0** | **3.0** | **5.0** |
| 1 | | 16.3 | 16.3 | 21.9 | 21.3 | 2.2 | 2.3 | 2.8 | 2.9 | 0.63 | 0.62 | 0.51 | 0.52 |
| 2 | | 19.7 | 19.7 | 23.0 | 20.1 | 2.5 | 2.5 | 2.9 | 3.1 | 0.63 | 0.62 | 0.57 | 0.53 |
| 3 | | 20.0 | 19.1 | 22.8 | 22.1 | 2.0 | 2.0 | 2.5 | 2.6 | 0.63 | 0.64 | 0.54 | 0.51 |
| 4 | | 13.1 | 13.9 | 15.2 | 19.7 | 2.3 | 2.4 | 2.6 | 3.0 | 0.59 | 0.59 | 0.53 | 0.50 |
| 5 | | 16.3 | 17.9 | 17.5 | 22.5 | 2.5 | 2.5 | 2.6 | 3.0 | 0.58 | 0.57 | 0.55 | 0.50 |
| 6 | | 17.9 | 18.1 | 20.1 | 19.6 | 2.5 | 2.5 | 2.7 | 3.0 | 0.57 | 0.54 | 0.50 | 0.46 |
| 7 | | 16.0 | 17.0 | 15.6 | 21.9 | 2.4 | 2.4 | 2.6 | 3.1 | 0.59 | 0.59 | 0.53 | 0.47 |
| 8 | | 15.1 | 16.0 | 17.3 | 19.4 | 2.9 | 3.1 | 3.2 | 3.4 | 0.53 | 0.50 | 0.47 | 0.45 |
| 9 | | 11.4 | 13.3 | 16.6 | 20.6 | 2.0 | 2.0 | 2.4 | 3.1 | 0.69 | 0.68 | 0.62 | 0.51 |
| 10 | | 9.4 | 10.2 | 11.0 | 18.7 | 1.7 | 1.7 | 1.9 | 2.4 | 0.69 | 0.68 | 0.64 | 0.54 |
| 11 | | 17.1 | 17.3 | 19.1 | 18.4 | 2.4 | 2.4 | 2.6 | 2.7 | 0.57 | 0.55 | 0.53 | 0.49 |
| 12 | | 14.0 | 15.7 | 12.6 | 20.2 | 2.4 | 2.5 | 2.7 | 2.9 | 0.64 | 0.63 | 0.59 | 0.57 |
| 13 | | 14.8 | 14.5 | 14.4 | 16.4 | 2.7 | 2.7 | 2.8 | 3.0 | 0.53 | 0.53 | 0.51 | 0.48 |
| 14 | | 14.6 | 14.5 | 13.6 | 18.3 | 2.5 | 2.5 | 2.6 | 3.0 | 0.61 | 0.58 | 0.58 | 0.51 |
| 15 | | 13.3 | 14.0 | 26.4 | 19.4 | 2.0 | 2.1 | 2.3 | 2.5 | 0.63 | 0.62 | 0.58 | 0.56 |
| 16 | | 15.3 | 15.7 | 23.3 | 25.5 | 1.8 | 1.8 | 2.2 | 3.0 | 0.58 | 0.58 | 0.50 | 0.43 |
| **Average:** | | 15.3 | 15.8 | 18.1 | 20.3 | 2.3 | 2.3 | 2.6 | 2.9 | 0.61 | 0.60 | 0.55 | 0.50 |
| **Standard deviation** | | 2.69 | 2.34 | 4.30 | 2.04 | 0.32 | 0.33 | 0.28 | 0.24 | 0.04 | 0.05 | 0.04 | 0.04 |

The registration results are fairly consistent, as indicated by the results and their standard deviations shown in Table 1. Adding noise to landmark locations has only modest effects on these metrics. The Hausdorff distances both increase by about 25% between no error and 5mm$^2$ error, and the Dice coefficients decrease modestly. This consistency is unfortunately not purely a result of the method's robustness; there are limitations in the suitability of these metrics for assessment of a spinal model. The maximum Hausdorff distance corresponds to the single point on the visualization with the largest distance to the ground-truth. The spine is a large anatomic structure, with many processes capable of semi-independent shape and pose variability. This produces many opportunities for a single large Hausdorff distance to occur. The average Hausdorff distance and Dice coefficients provide a more general measure of a registration's accuracy, but this generality not ideal for scoliosis assessment. The angle of curvature and overall impression of scoliosis can be obtained from the posterior vertebral anatomy, the laminae and processes. These anatomic structures are small relative to the vertebral bodies. Therefore, an informative visualization with accurate posterior anatomy may have a high average Hausdorff distance or low Dice coefficient, if the vertebral bodies do not align with the ground-truth. Likewise, accurately registered vertebral bodies can result in low average Hausdorff distances and high dice coefficients even if the posterior anatomy is inaccurate.

Clinical scoliosis assessment is not concerned with Hausdorff distances or Dice coefficients. Scoliosis assessment requires the angle of coronal curvature, and visualization for treatment design. Figure 23 shows four visualizations generated from landmarks without added noise. Distance maps are imposed on the visualizations, where the color maps to the distance from that point on the visualization to the corresponding point on the ground-truth segmentation. The Cobb angle was also measured from the endplates of the resulting visualizations, for each amount of landmark noise, and compared with ground-truth. The absolute value of the error between ground-truth and visualization angles is used as an assessment metric. It describes how well the visualizations capture scoliotic deformation at the full-spine scale.

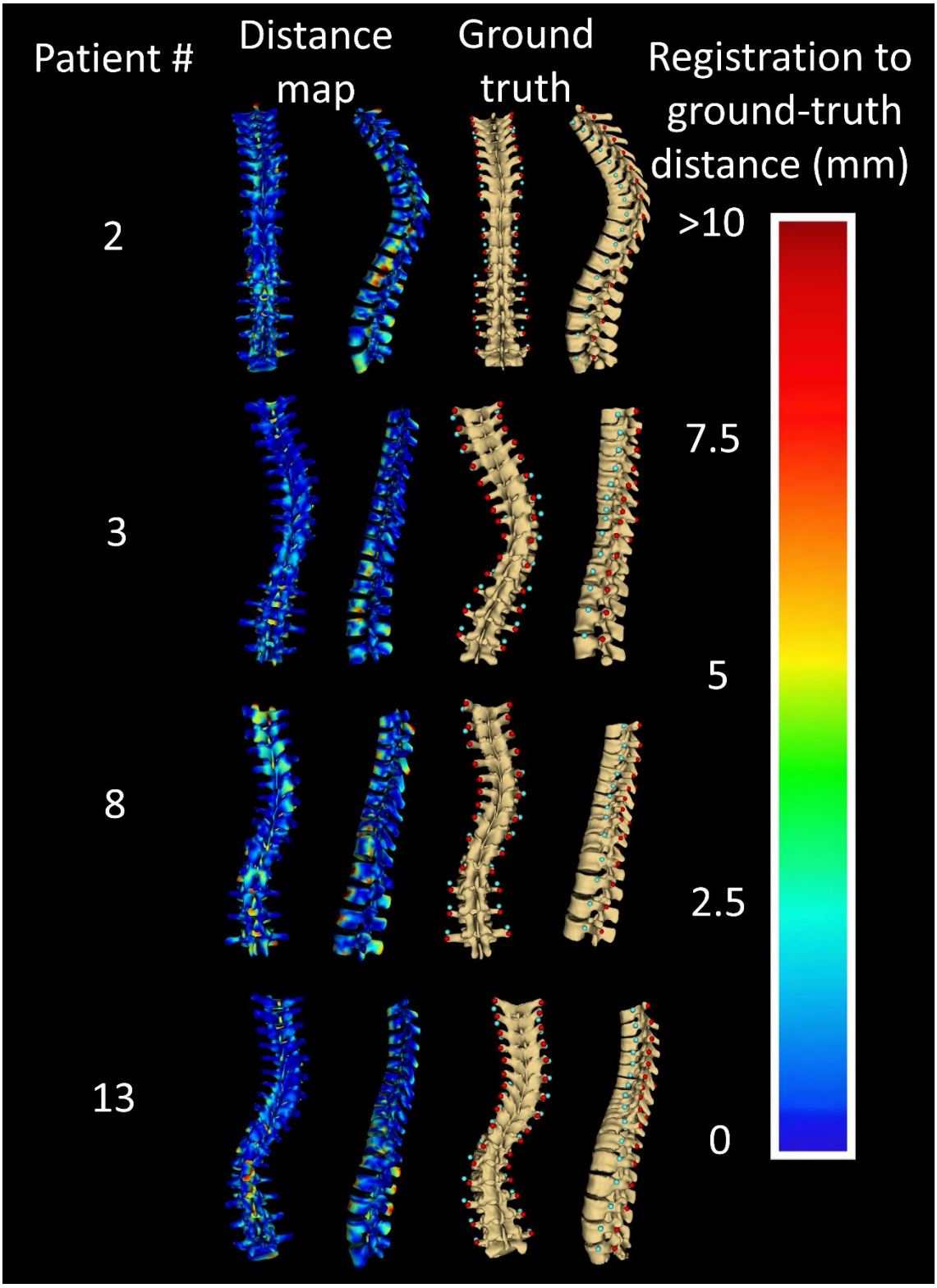


**Figure 23: Distance maps depicting registration accuracy compared with CT derived ground truths with transverse process landmarks (red) and supplemental anchor points (blue)**

The distance maps shown in Figure 23 give a positive qualitative impression of the results with respect to their utility for scoliosis assessment. Different patient-specific 3D deformations are seen in the visualizations when compared to the healthy shape. The forward curvature of patient #2's kyphosis, and the single and double curves of varying degrees exhibited by the other patients are conveyed by the visualizations. The posterior surfaces of the vertebrae are usually the most accurately registered regions. This is unsurprising since the nearby skeletal landmarks have a greater effect on the resulting visualization, and these landmarks are accurate by virtue of their manual identification. The accuracy of the posterior surface is particularly relevant for scoliosis assessment. This is the direction from which scoliosis is typically assessed with X-ray. The visualizations should be should be especially accurate from this direction, this accuracy is shown in the posterior views in Figure 23.

Several noticeable regions with higher error are visible on the distance maps of Figure 23. These regions of error generally belong to one or both of two categories: regions at the top and bottom boundaries of the spine, or regions anterior or posterior to the transverse processes, on the vertebral bodies or spinous processes, respectively. These inaccuracies are primarily the result of how the healthy-shaped model warping is constrained. Regions at the boundaries of the spine have lower average landmark and anchor point densities. Therefore, they do not tend to conform as closely to patient anatomy. This type of inaccuracy does not impair scoliosis assessment since the boundary of an ultrasound scan will not be in the middle of a region of interest. The errors on the spinous processes are also likely the result of being removed posteriorly from the landmarks. These inaccuracies are small, as the rest of the given vertebra is generally unaffected. Finally, the inaccuracies on the vertebral bodies can be attributed to constraint provided by the anchor points. The use of anchor points improves results substantially, but they represent anatomic information which has been inferred from limited physical landmark information. They are therefore limited representations of actual patient anatomy and subject to inaccuracies. Fortunately, these errors are also of secondary importance for scoliosis assessment. They are small, normally confined to one side of several vertebrae, not affecting the overall shape of the spine.

Some of the remaining inaccuracy in the vertebral bodies may be due to the scaling of the registration. The magnitude of the distance between a transverse process landmark and its corresponding anchor point only reflects the overall scale of the patient's spine relative to the healthy-shaped model. Therefore, rapid changes in transverse process width, such as the thoracic to lumbar transition of patient #2, or unusually wide or narrow transverse process can result in registrations with unusually wide or narrow vertebral bodies. The width between transverse processes and the depth and height of vertebral bodies can vary somewhat independently. This makes it challenging to formulate a scaling factor to impose on the anchor points' offset entirely from the geometry of the transverse process landmarks. Limitations of this scaling technique may account for the unimpressively large yet surprisingly consistent Dice coefficients listed in Table 1. Although these scoliotic patients were generally adolescents, and the healthy-shaped model was derived from an adult, the vertebrae of the healthy-shaped model are smaller, particularly in the vertebral bodies. This is may be the result of the method used to segment the healthy CT, or morphologic operations applied after such as excessive smoothing. The result is that when the healthy-shaped model is registered and scaled to patient anatomy, the vertebral bodies are consistently enveloped by the those of the patient's ground-truth. The difference in size accounts for the low Dice coefficients while allowing them to be consistent.

The various registration metrics and inaccuracies described above are informative considerations here for validation, but unimportant in scoliosis assessment. The visualizations with distance maps in Figure 23 give an overall impression of the results' quality, albeit a largely qualitative one. The ability of the visualizations to produce the patients' Cobb angles provides a quantitative assessment of the accuracy of the visualizations with specific reference to scoliosis assessment. Cobb angles were measured from posterior views of the patients' CT segmentations, and their corresponding visualizations, for each amount of landmark noise. The absolute differences between the ground-truth segmentations' Cobb angles and those of the visualizations were calculated, and are listed in Table 2.

**Table 2: Patients' ground-truth Cobb angles measured from CT, and Cobb angle error absolute values for each patients' visualizations with increasing landmark position noise**

| Patient # | Ground-truth angle (degrees) | Cobb angle absolute error (degrees) | | | |
|---|---|---|---|---|---|
| | | 0.0mm² noise | 1.0mm² noise | 3.0mm² noise | 5.0mm² noise |
| 1 | 40.3 | 4.1 | 3.1 | 6.3 | 4.9 |
| 2 | 5.9 | 4.4 | 2.8 | 4.9 | 7.2 |
| 3 | 59.0 | 0.4 | 2.7 | 5.5 | 6.7 |
| 4 | 31.3 | 2.9 | 5.6 | 11.4 | 29.9 |
| 5 | 45.3 | 6.1 | 5.1 | 0.7 | 0.7 |
| 6 | 30.9 | 2.0 | 1.8 | 2.1 | 12.2 |
| 7 | 35.6 | 0.9 | 1.1 | 15.9 | 28.4 |
| 8 | 51.2 | 1.3 | 1.1 | 16.0 | 8.8 |
| 9 | 12.2 | 0.1 | 6.7 | 9.7 | 3.8 |
| 10 | 9.6 | 7.8 | 3.7 | 0.7 | 13.6 |
| 11 | 29.7 | 1.0 | 0.3 | 8.7 | 18.3 |
| 12 | 29.2 | 1.9 | 5.8 | 16.5 | 9.4 |
| 13 | 55.6 | 13.8 | 1.4 | 12.6 | 21.1 |
| 14 | 38.1 | 5.0 | 3.3 | 10.9 | 7.6 |
| 15 | 42.9 | 7.6 | 0.3 | 4.5 | 15.4 |
| 16 | 67.1 | 0.7 | 3.4 | 6.7 | 3.5 |
| **Average** | | 3.8 | 3.0 | 8.3 | 12.0 |
| **Standard deviation** | | 3.6 | 1.9 | 5.1 | 8.4 |

The data in Table 2 largely support the suitability of this method for visualizing scoliosis, given a condition. The condition for the suitability of these visualizations for scoliosis assessment is that the landmark locations are normally distributed about true landmarks with a standard deviation of not much more than 1mm$^2$. The most notable Cobb angle error measurements from the noiseless landmarks is that of patient # 13. This was partly because of the large magnitude of the curve, which was partly smoothed out by the thin-plate spline registration. Nonetheless, the magnitude of the curve remained above the threshold for surgery of 40°. Sudden changes can be seen in a given patient's Cobb angle errors with small changes in the amount of noise added to their landmark locations, like patients # 7, #8, #13, and #14 for example. This occurs

when noise added to the landmarks belonging to the end vertebrae, which define the angle of curvature, acts to change this angle. The angle may change substantially if the vertebral endplates are deformed by the noise. A familiar operator will not measure an angle from a clearly deformed endplate; they will either recollect data or estimate the plate's true orientation from nearby anatomy. Furthermore, up to $1mm^2$ noise standard deviation, other errors are usually within 5°, roughly the variability in radiographic Cobb angle measurement reported by [30]. This is a quantitative indication that the overall deformation of the spine is captured by this visualization method, indicating its suitability for scoliosis assessment.

### 3.6 Summary

This chapter presents a method for producing spinal visualizations depicting 3D patient-specific scoliotic deformity. The method can operate entirely with the use of ultrasound data, and one healthy-shaped spine model. The method was designed with the transvers process landmarks in mind. They have a clear characteristic response in ultrasound, and have been used to accurately estimate coronal curvature. The method employs a thin-plate spline to estimate continuous 3D deformation from healthy-shaped model to patient landmark registration. The transverse processes lack sufficient distribution towards the vertebral bodies to specify deformation in that direction. A technique was developed to compute this direction from landmark geometry and supplementing natural skeletal landmarks with anchor points in that direction. The thin-plate spline registration performed on the transverse process landmarks plus anchor points then realistically captures the continuous deformation of the spine.

To validate the method, 16 sets of transverse process locations were taken from patients' CTs. Visualizations were generated using the proposed method. Spines manually segmented from the patient CTs were the ground-truths to which the visualization were compared. It is difficult to describe the accuracy of the resultant visualizations using a few parameters. Regardless, Hausdorff distances and Dice coefficients are reported for the visualizations. Distance maps, colorizing the magnitude of the distance between the visualization and ground-truth at each point on the visualization, are more representative, if qualitatively, of the method's accuracy.

# Chapter 4

## Automatic landmark generation from ultrasound scan segmentation

To generate visualizations using the method from Chapter 3, the transverse process locations are the only patient data required. Therefore, manually locating each of these landmarks contributes substantially to workflow time. To the end of reducing the time and interaction required from the operator seeking to produce visualizations like those of Chapter 3, this chapter presents a method for deriving skeletal landmark locations from an ultrasound scan.

The difficulties in interpreting ultrasound scans, covered in Chapter 2, can lead to numerous problems with manual landmark identification. Landmarks can be missing from simple difficulty in interpreting images containing the landmarks, but incomplete scans are also a possibility. Both Cheung *et al.* and Wang *et al.* mention being unable to locate all of the required landmarks on some patients and having to discard data. This is more likely in scoliotic patients where vertebrae can be rotated to orientations making the landmark surfaces invisible to ultrasound, and in patients with higher BMIs where fat tissue degrades the image quality. Landmarks can also be placed incorrectly; a rib can be mistaken for a transverse process since they both extend laterally from the spine and have similar surface profiles.

In cases where a human operator is unable to produce defect-free landmark sets for registration, it is unlikely that a single-step automatic landmark generation algorithm will either. To bridge the gap between imperfect landmark sets, produced either by a human or the automatic method described below, a Slicer module was developed which offers various operations to correct common defects in such a landmark set. These operations are described after the ultrasound segmentation and initial automatic landmark estimation methods.

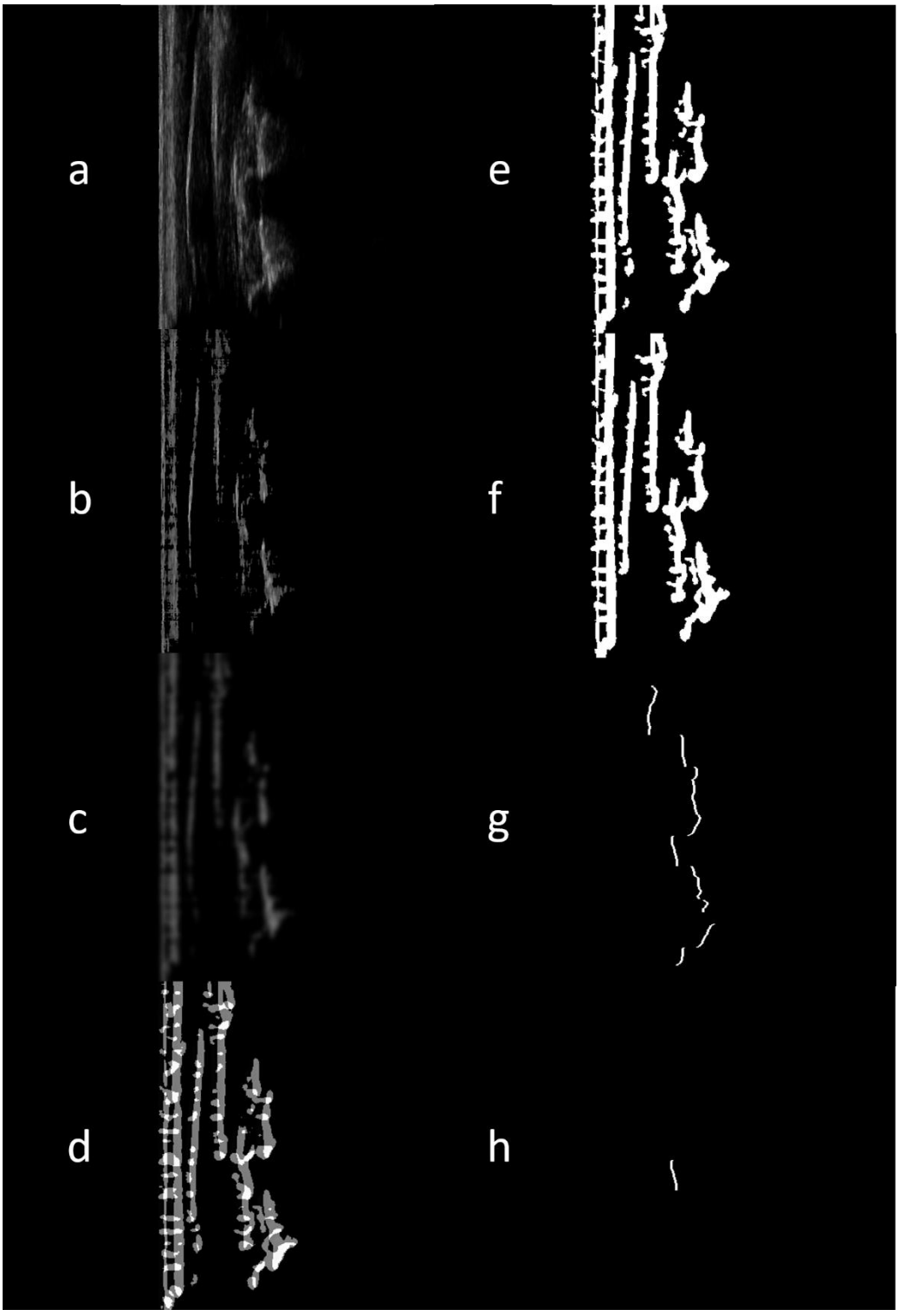


**Figure 24: (a) - Original parasagittal image (b) - After threshold (c) - After Gaussian smoothing (d) - Sobel edge detection (e) - Binary image for morphology (f) - After island removal (g) – After scanline-based pixel removal (h) – After shadow-based pixel removal**

## 4.1 Ultrasound segmentation

The method for automatic landmark generation uses a bone surface segmented from ultrasound as input. A bone segmentation method specifically designed to identify the transvers processes was recently integrated into PLUS. PLUS is an open-source software package for ultrasound imaging and processing [55]. PLUS allows image segmentation to be performed automatically, during or after scanning, in a pipeline to 3D Slicer [56], the environment where the landmarks are subsequently generated and the visualizations of Chapter 3 are produced. The segmentation method was adapted from Kamali2017 *et al.* [57]. The adapted segmentation method comprises three main steps: ultrasound image filtering, possible bone surface identification, and false-positive bone surface removal. These steps are depicted in Figure 24 and subsequently described in more detail.

To improve regularity in the images to be passed to the segmentation method, thresholding and Gaussian smoothing filters are first applied. The threshold filter sets all pixel values below a threshold, determined by the standard deviation of pixels in the same image row, to zero. Since bones will be identified with an edge detector, this threshold prevents ultrasound speckle or other locally bright spots from being wrongly identified as bone. The Gaussian smoothing further reduces the impact which small, high-frequency features have on the output. Possible bone surfaces are then identified with a Sobel edge detector which computes the numerical derivative along rows and columns of pixels. Three steps are then employed to remove pixels falsely identified by the edge detector as bone: island removal, scan-line based removal, and bone shadow examination. Island removal simply checks how many pixels are contiguous within a group and removes them all if the group is small. Scan-line based removal uses knowledge of the fact that, once a bone surface is encountered by the ultrasound wave, nearly all of the signal is returned to the transducer and certainly no other bone surfaces beneath the first will be detected. Scan-line based removal then discards bone pixels above the last candidate bone pixel that is encountered along a scan-line. The final step of false positive removal and the overall segmentation method is to examine the areas beneath the

possible bone surfaces. Bone surface pixels should have dark acoustic shadows beneath them, and if not, the pixels are not likely to be bone and are removed. This step is illustrated in Figure 25.

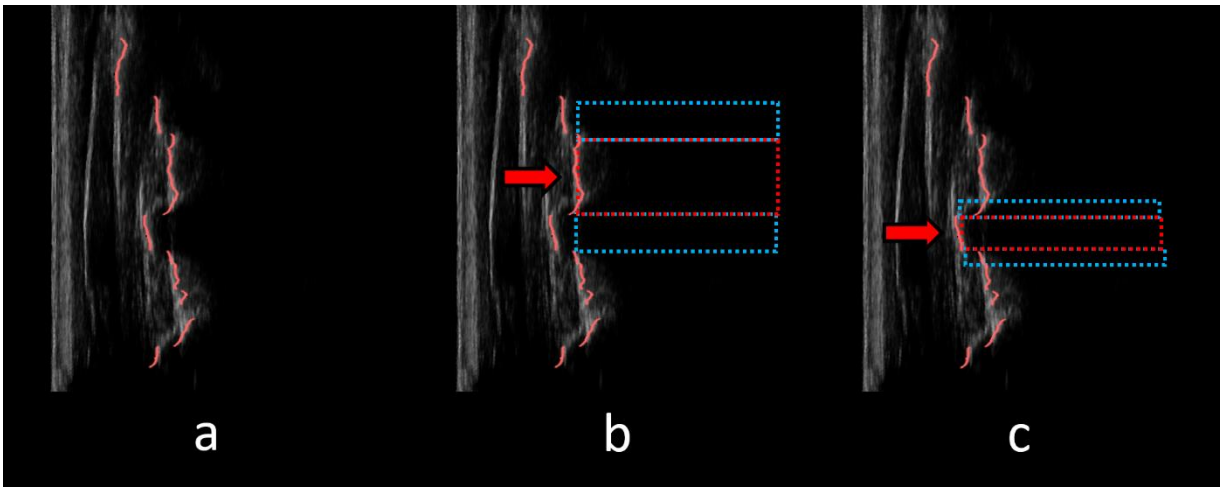


**Figure 25: (a) - Red candidate bone surfaces superimposed on original ultrasound image (b) - False potential bone segment shadow comparison (c) - True bone segment shadow comparison**

As shown in Figure 25, the candidate bone shadow is taken as the entire area beneath the bone surface, to the end of the image. The average brightness in this area, red in Figure 25, is compared with the average brightness of two areas beneath either side of the bone surface, each half the width of surface, blue in Figure 25. If the candidate shadow area is brighter than either area next to it, then it is apparently not an acoustic shadow and the candidate bone pixels above it are apparently not bone and are therefore removed. The final bone surfaces segmented from this ultrasound image are shown in Figure 26. A volume reconstructed from all of the pixels segmented from a scan is shown as a surface in Figure 27.

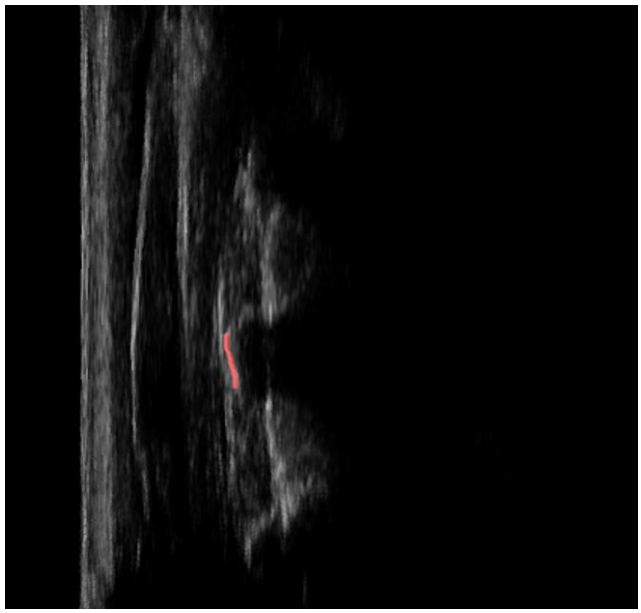

**Figure 26: Red line shows pixels segmented as bone, superimposed on original ultrasound image**

The nature and quality of the bone surface naturally depends on the particular segmentation algorithm used to produce it. There are many methods to choose from for segmenting bone in ultrasound, however, the adaptation of the method from Kamali *et al.* offers two distinct benefits. The primary benefit, as mentioned above, was from the convenience possible with the method; it was recently integrated into PLUS. The second benefit is from the final, false-positive removal step where candidate bone surfaces' acoustic shadows are examined. This technique is specifically designed for the profile which transverse process produce in a parasagittally oriented ultrasound scan. The regular spacing of the bone surfaces provides a heuristic for determining whether a region under a bright surface is indeed likely to be an acoustic shadow, as exemplified in Figure 26. This improves the results of this method with respect to the transverse processes, if at the expense of its generality; the method would be unable to segment a single, large bone surface occupying more than half the image width. More details on the Kamali *et al.* approach can be found in [57].

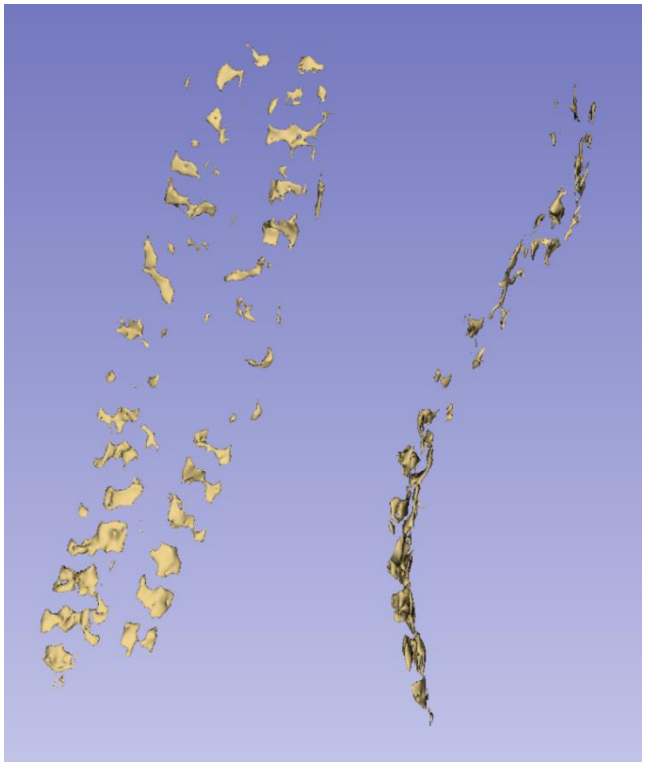

**Figure 27: Posterior and left views of spine surface segmented from ultrasound using method adapted from [57]**

### 4.2 Initial landmark estimation with *k*-means

A binary label map representation of the bone segmentation image consists of many points in 3D, each with a value, either 0 or 1, depending on whether the point belongs to the segmentation. Therefore, reducing the segmentation to one point per landmark amounts to a problem of under-sampling these point locations. A *k*-means algorithm was adapted to provide an initial estimate of landmark locations from an ultrasound segmentation. *k*-means normally requires that either *k* be known, or some error criteria for termination be

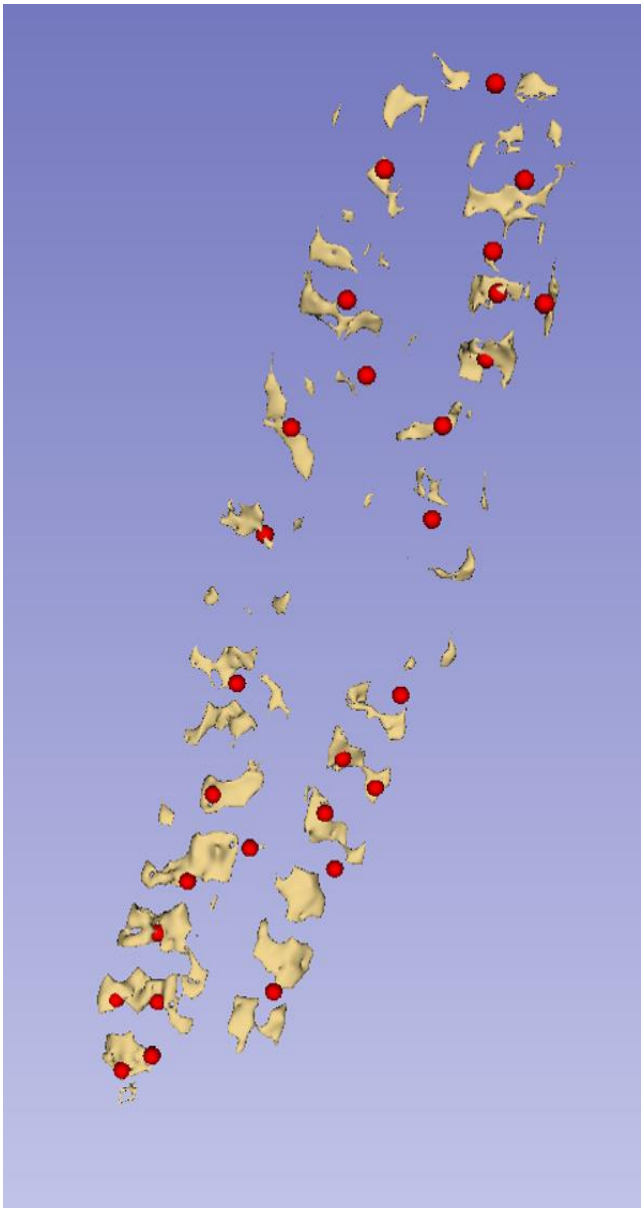

**Figure 28: Red landmarks from *k*-means method performed on shown ultrasound segmentation**

specified. This adaptation relaxes the assumption regarding *k*, so the user is not required to specify the number of transverse processes present or visible in the scan, or specify termination criteria. *k*-means is adapted by iterating it with *k* increasing from 1 to 34 in search of the best landmark estimate of the segmentation, and by modifying its error function. Iteration is bounded at 34 as the maximum number of landmarks possible with two at each vertebral level in a thoracolumbar scan. If more of the spine were to be included, this limit is simply raised. Increasing *k* will always produce a better approximation of the segmentation, so to prevent unfair preference for larger *k* values, *k*-means' error function was multiplied by *k*. This is not mathematically equivalent to cancellation of the error reduction produced by adding another point to the landmarks, but serves as a heuristic to allow estimates with other than 34 landmarks. The *k*-means algorithm was implemented using vtk's vtkKMeansStatistics class, and the default random initial locations of the *k* means was not modified. Therefore, the final landmark locations output by the algorithm will not be consistent, but an example output is shown on the segmented surface in Figure 28. The method produced variable numbers of landmarks in variable locations, usually produced 28-34 landmarks from the segmentation shown in Figure 28, for example.

## 4.3 Landmark set repair

In order to produce a visualization in the manner described in Chapter 3, precisely one pair of right-left symmetric landmarks is required for each vertebra. The landmarks resulting from this method, shown in Figure 28, deviate from this requirement in several manners. This method sometimes places multiple landmarks on a single side of a given vertebral level, as can be seen towards the upper-right and lower regions of the segmentation. Outlier landmarks may be placed medially or laterally from the transverse processes if points are skewed by nearby surfaces, possibly the result of laminae or rib segmentation. Also, intervals of the scan may lack landmark points, as can be seen midway up the segmentation in Figure 28, where the segmentation algorithm recognized less bone surface. Fortunately, these defects can largely be corrected with geometric analysis, owing to the bilateral and axial (inter-vertebral) symmetry which *k*-means still roughly captures from the segmentation.

A Slicer module was developed which offers functionality to repair these varieties of defects in *k*-means' initial landmark estimations. Operations to consolidate those points which mark a single landmark multiple times, recognize intervals with omissions and impute points correspondingly, and to recognize and delete outlier points too lateral or medial to be likely to correspond to the desired skeletal landmarks. The distinction between normal landmarks and defects requires quantification for each test. User-configurable parameters are controlled with sliders through the module's interface. The segmentation and landmarks from Figure 28 are shown with the Slicer module interface in . Each of the reparation operations makes use of bilateral symmetry to treat each side of the spine separately. Therefore, a method for classifying points as belonging to the right or left side of the spine was developed and is subsequently described, before describing the side-wise reparation operations.

### 4.3.1 Right-left landmark classification with sliding k-means

The rough bilateral symmetry of the landmarks output by the previous *k*-means algorithm, and used by the visualization method of Chapter 3, make classification of landmarks as belonging to the right or left side possible and desirable, respectively. This is accomplished with another variation on the *k*-means algorithm.

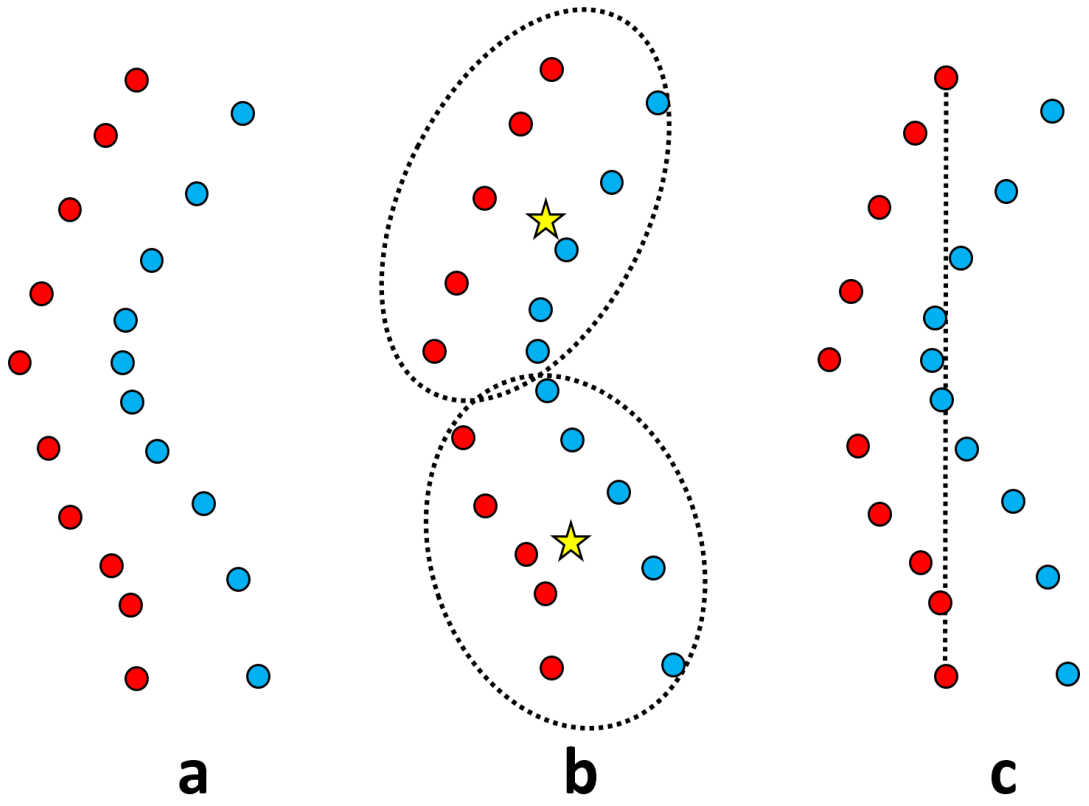


**Figure 29: (a) - A hypothetical set of bilateral spinal landmarks, their true sidedness indicated by their color (b) - Illustration of the failure of the radial basis of *k*-means to correctly classify the points as right or left (c) - Illustration that landmark sets exhibiting sufficient curvature cannot be linearly classified as left or right**

Simply performing *k*-means on a set of transverse processes will not correctly classify points as left or right sided. Consider Figure 29a, a pair-wise complete set of vertebral landmarks where their color denotes their true sidedness. Performing *k*-means on the group of points as a whole, with $k = 2$ might classify the points as shown in Figure 29b. Figure 29c illustrates that, in cases with sufficient curvature, no linear scaling can compress the axial distribution of the points into two groups which may be correctly classified as left-right. To make right-left classification with *k*-means possible, the landmarks are first sorted, superior-most to inferior-most. The *k*-means algorithm, with $k = 2$ for right-side versus left-side, is then performed on the first *n* points where *n* is a user-configurable window size parameter. The window then slides down, leaving the superior-most point, and incorporating the next inferior-most point, and *k*-means is performed again. The window size, *n*, should be small enough that the points it contains are a short enough segment of the

spine so as to be nearly straight, and therefore linearly separable. Too small of a window, however, may result in incorrectly classified points, especially at boundaries with omissions. A window size of 5 landmarks was found to consistently classify left from right sided landmarks for the results in this chapter. This sliding-window procedure is illustrated in Figure 30. Diamond-shaped points are those currently in the window, and stars represent possible locations for the two means. Since a single iteration of *k*-means may incorrectly classify a point, the result of each iteration constitutes one 'vote' for which side the point belongs to. Naturally, if a point's mean is the right-most of the two means, the point receives a vote for the right, and similarly for the left. Like sorting the points from superior to inferior, this requires knowledge of the patient's anatomic directions. Correspondence between directions in the virtual 3D Slicer environment where the landmarks are repaired, and the patient's physical directions can be ensured by correctly orienting the reference position sensor on the patient.

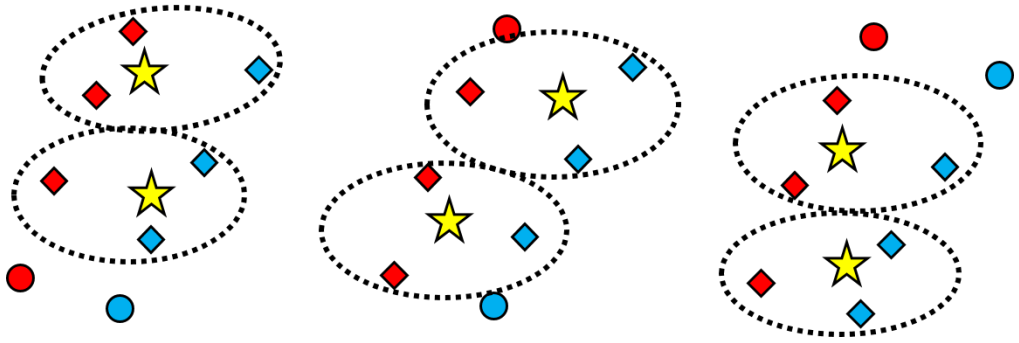

**Figure 30: The first 3 iterations of sliding *k*-means performed on the landmark set of Figure 29**

### 4.3.2 Duplicate landmark identification and consolidation

Figure 31a shows a hypothetical set of points from along one side of a spine. Blue points are those being tested as possible duplicates. The diamond points represent where one landmark has been marked twice by *k*-means, that is, a true duplicate which this method seeks to identify. This kind of duplication is often characterized by a deviation from normal axial symmetry. That is, duplicate points tend to be 'beside' other points rather than 'after' others. It is deviation from axial symmetry which allows these colloquial terms to be implemented in more precise mathematical terms. Each pair of points is tested as a candidate duplicate

pair. To test a point pair, the vector joining the pair is computed as a candidate duplicate direction. A reference direction is computed as the vector joining the points just above and below this candidate pair. The angle between the reference vector and the candidate duplicate vector is computed.

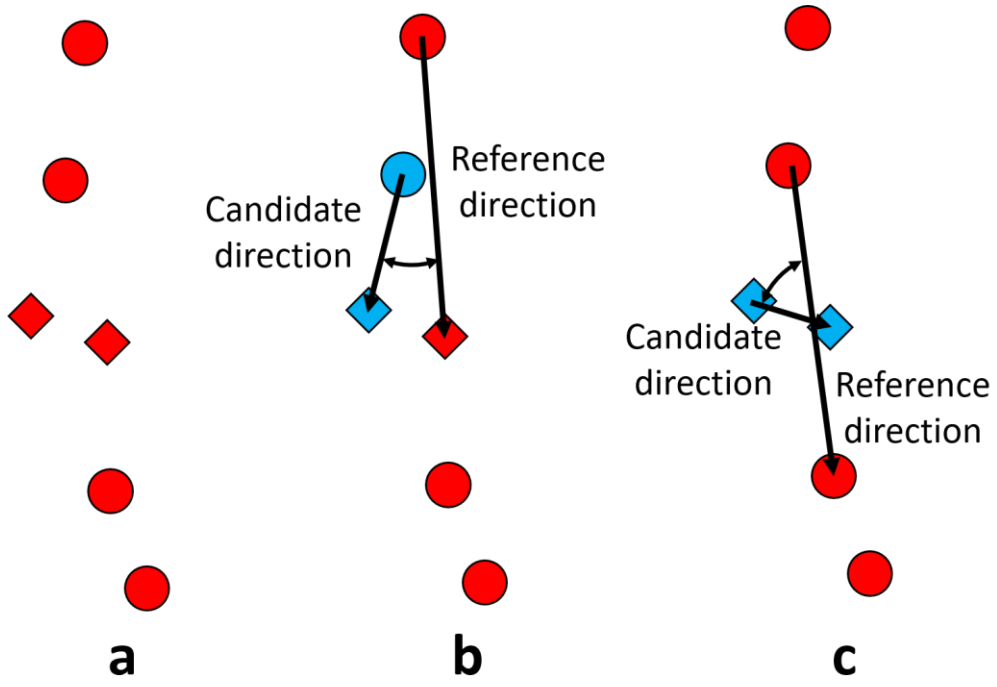


**Figure 31: (a) - Hypothetical points identified as landmarks along one side of a spine, diamonds indicating where one landmark is marked twice (b) - A pair of points (blue) from different vertebral levels are tested as possible duplicates (c) – A pair of points from the same vertebral level (true duplicates) are tested**

Figure 31b illustrated that this angle tends to be small when both of the points come from different vertebral levels. Figure 31c, by contrast, shows how this angle increases when points are placed 'beside' one another at a given vertebral level. If this angle exceeds a threshold, then the points are recognized as duplicates and they are replaced with their average position. This threshold user-configurable in the Slicer module, and is set to 45° by default, as the angle at which the points are more 'beside' one another than 'after' one another. Figure 32 shows the result of a single iteration of this method on the landmarks of Figure 28.

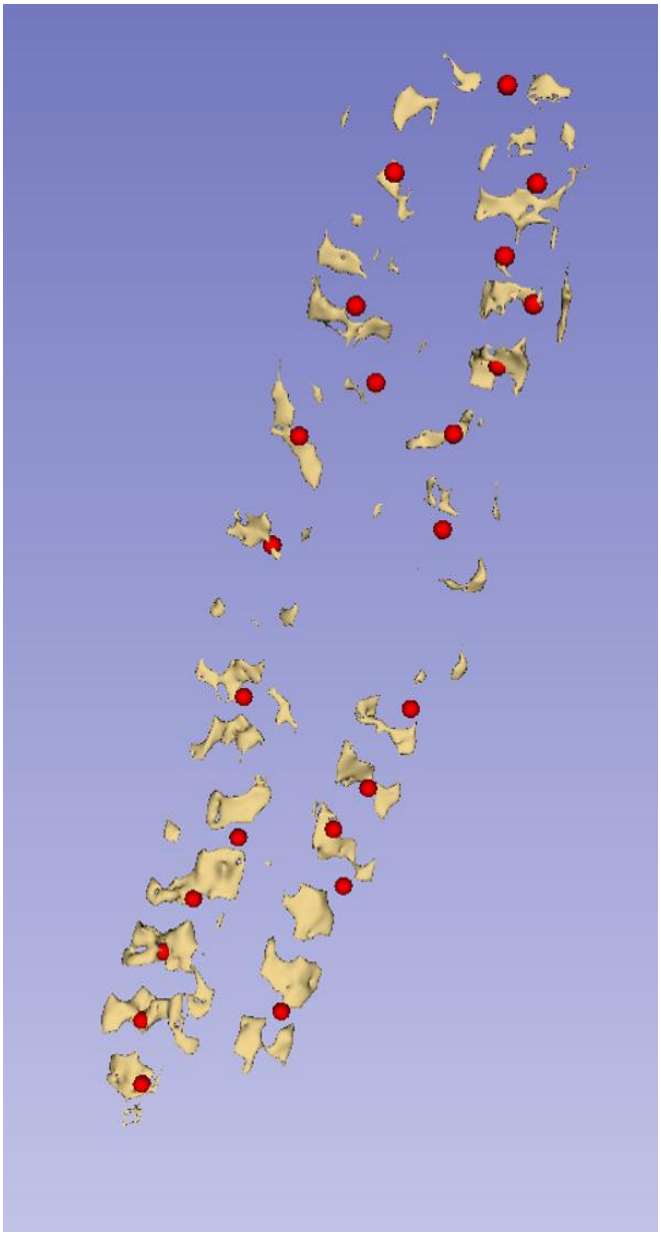

**Figure 32: Automatically generated landmarks of Figure 28 after duplicate consolidation**

### 4.3.3 Omission detection and imputation

Intervals along either side of the spine where landmarks are absent are identified on the basis of the length of the intervals between landmarks compared with inter-landmark distances both nearby the interval in question, and with interval lengths along the entire side of the spine. To quantify the lengths of inter-landmark intervals, polynomial fits to both sides' landmarks were used as a geometric representation. The superior-inferior coordinates of the existing landmarks were used as the independent variable in the polynomials, and the anterior-posterior and right-left coordinates were the dependent variables. Interval lengths were then assessed based on other interval lengths. Unexpectedly large intervals would then signify omitted landmarks.

A given interval is deemed to be unexpectedly large if it is longer than either of them by some amount. To compare a given interval's length to that of the rest, a polynomial is fit to the interval length values versus the total length along the spine at which the interval occurs. This gives each interval along the spine a fit error for the polynomial. An interval is identified as having omitted landmarks on the basis of this polynomial if its fit error is larger than some amount related to normal interval length fit errors. For the sake of robustness of design, this amount is the average interval fit error, plus the product of the interval fit error standard deviation times a user-

configurable specificity. Since this parameter is added for robustness, it is set to 1 by default, exerting no effect on the equation, unless the operator chooses to change it. The polynomial approach was chosen because it gives more weight to local information while still considering more of the overall structure of the landmarks. The inter-landmark intervals tend to be shorter in the upper thoracic spine and longer in the lumber spine, corresponding to the lengths of the vertebrae. Therefore, local inter-landmark intervals are better indications of the expected length of a given interval and should be given more weight.

Once an interval is identified as having omitted landmarks, points must be imputed into the interval to correct the omission. The module generates 'patches', one for each interval with omissions, points are added along the polynomial fit to original points' curve. Points are added to patches based on how much they would improve the interval length polynomial fit if they were included with the rest of the landmarks. Once the change in polynomial fit error corresponding to the inclusion of the new point is no longer large enough, imputation ceases. The threshold for this error reduction is -0.1 by default. Although this estimates how many points may be omitted in a given interval, the patch is not incorporated without the user's approval. The user makes the final decision regarding how many, if any, points will be included in the patch. Therefore, this patch point count estimation and its related parameter are for convenience only. To ensure the correct number of points are included in each patch, the user may add or remove points from each patch with the click of a button. Once the patches with the user-approved numbers of points are incorporated, the process may be iterated as interval statistics are more representative of a complete landmark set and the interval omission algorithm may detect new omissions. The process of generating and imputing patches for intervals with omissions is illustrated with the example landmarks in Figure 33 and Figure 34, for left and right sides of the spine, respectively.

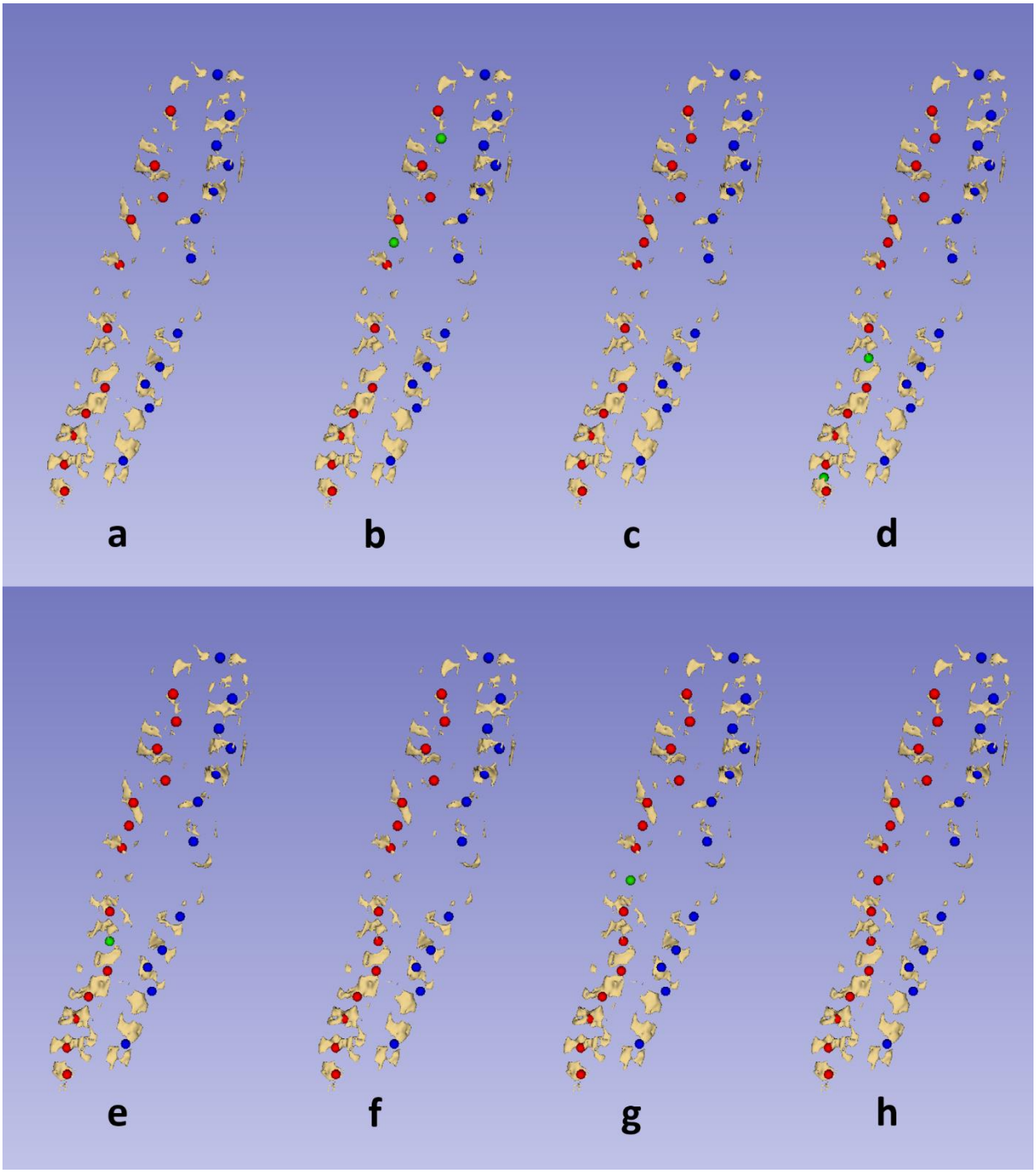


**Figure 33: Omission detection and imputation on the left side (a) – View from the posterior direction, the red points indicate that the left side is selected (b) – Green points shows first patches suggested my module (c) – Patches are incorporated with user's approval (d) – Patches are generated a second time (e) – Operator removes bottom patch (f) – Patch is incorporated (g) – Final patch generated (h) Final patch is incorporated, completing the left side**

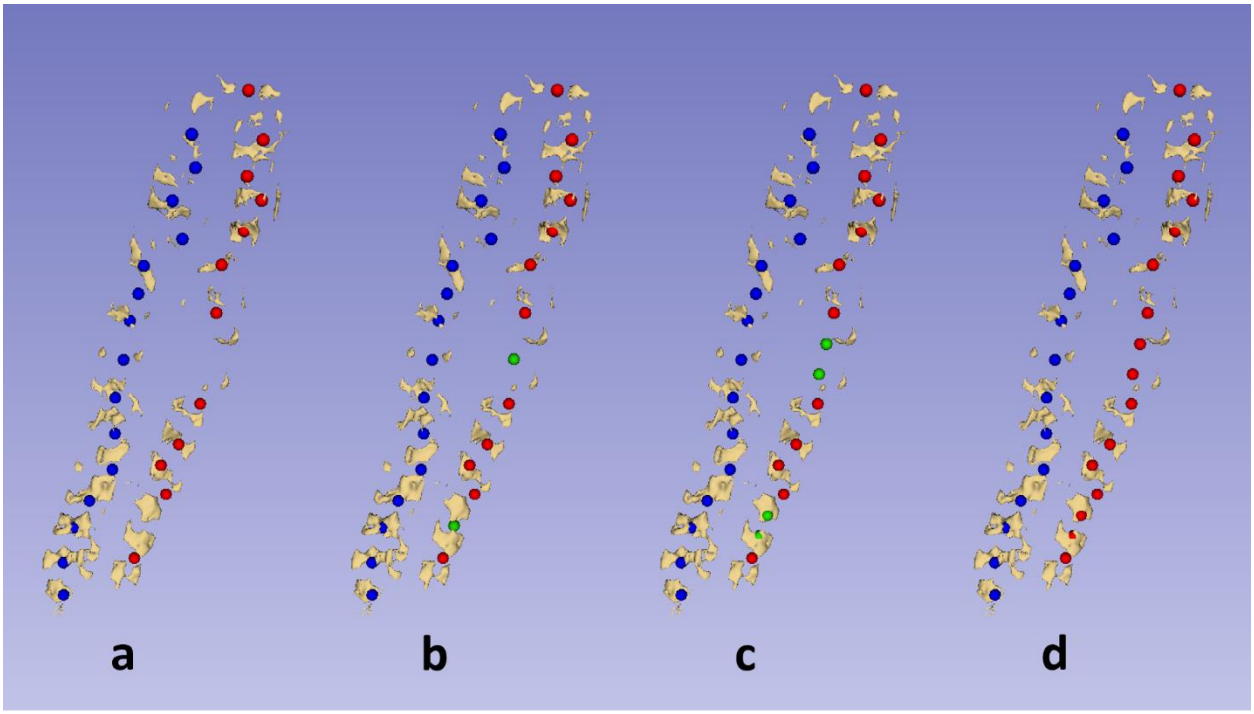


**Figure 34: Omission detection and imputation on the right side (a) – Red indicates right side is selected (b) – Patches are generated by module at user command (c) User decides to add a point to each patch, the module reorganizes the patches accordingly (d) – The patches are incorporated**

Figure 33a shows the same landmarks as Figure 32, those generated by *k*-means after duplicate consolidation. The red points indicate which side is selected for patch generation, the left. Figure 33b shows two green points, each belonging to a patch suggested by the module at the request of the operator. Figure 33c shows the patches incorporated after the operator deemed them as corresponding to physical landmarks. Figure 33d shows the next suggested patches. The bottom most patch does not seem to correspond to a landmark, and was deleted, resulting in the patch shown in Figure 33e. The operator was satisfied with this patch and incorporated it, resulting in the landmarks of Figure 33f. Figure 33g shows the last patch requested by the operator, which was judged accurate and is shown incorporated in Figure 33h. Figure 34 shows the process for the right side. Figure 34a shows two points, each belonging to a patch suggested by the module. Figure 34b shows the landmarks after the operator recognized multiple omissions in each interval, and added a point to each. Figure 34d shows the landmarks with all recognizable omissions imputed.

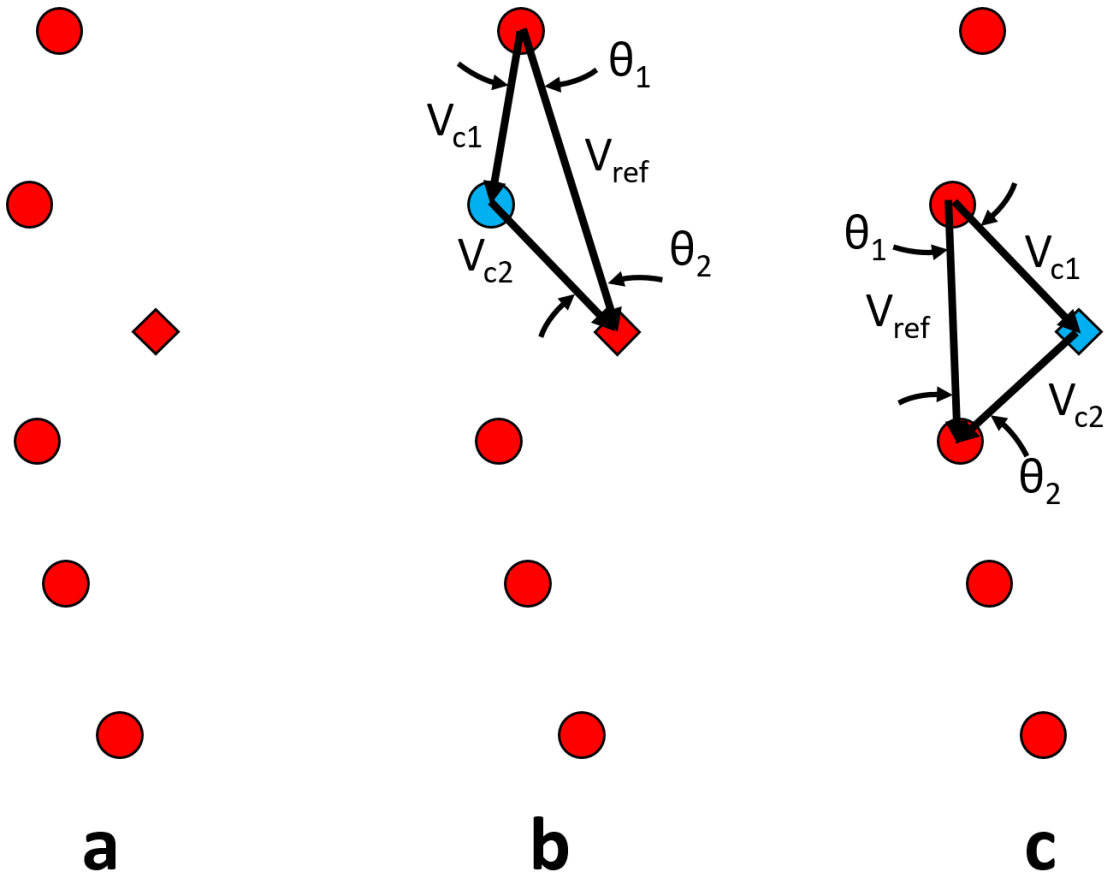


**Figure 35: (a) - Hypothetical landmarks along one side of the spine, diamond point is an outlier (b) - Characterizing one point (blue) with nearby inter-landmark vectors and angles (c) - The same characterization for the outlier point**

### 4.3.4 Outlier detection

As described at the beginning of this section, the types of outlier landmarks to be detected are those which deviate medially or laterally from the curve of correctly placed landmarks. Although these points are placed by *k*-means in this method, they may correspond to ribs, laminae, or structures other than the transverse processes intended to be segmented from the ultrasound scan. Such lateral or medial deviations are detected based on local inter-landmark vector angles. This is similar to the method for duplicate identification, but it tests individual landmarks rather than pairs. Two characterization vectors, compared with one reference vector, are used to decide whether or not the point is an outlier. One characterization vector is that which

points into the point from the landmark immediately above it, and the other one points out of the point into the landmark immediately below it. The reference vector points directly from the landmark above to the one below. If the angle which both of the characterization vectors form with the reference vector exceed a user-configurable threshold, then the point is determined to be an outlier. Outliers are removed and repetition of the operation may recognize more outliers if the geometry of the landmark set has improved. Choosing the ideal default value for the outlier detection angle threshold is challenging because it is not always clear which points are outliers. A user may even wish to delete a point actually placed on a landmark, if it seems inaccurate enough, with the hope of re-estimating it with omission imputation. The Slicer module uses a default value of 30°, however 23° was used for the results in this chapter, as described below. Figure 35 shows two points being tested as outliers with these vectors. Figure 36 and Figure 37 show outliers being removed from the left and right sides of the example landmarks, respectively.

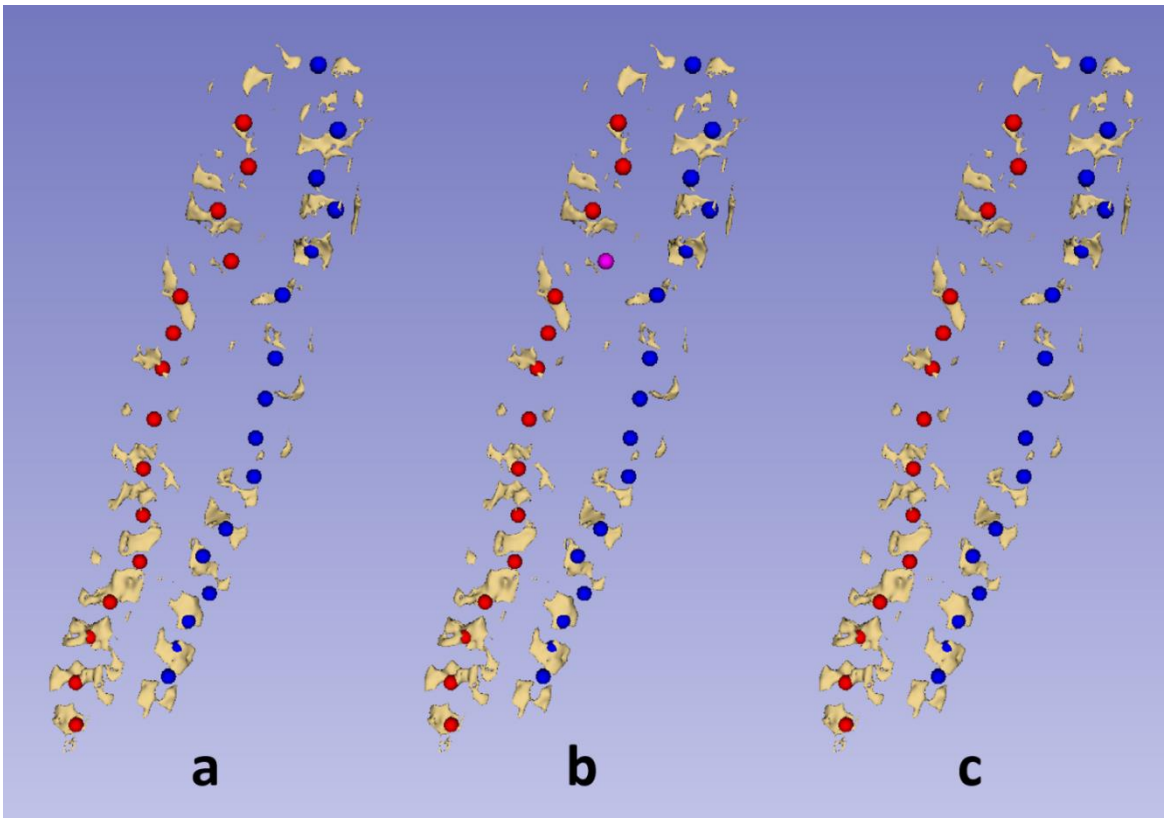


**Figure 36: (a) - Left side is selected after omission imputations (b) - Purple point indicates landmark identified as an outlier (c) - Outlier is removed**

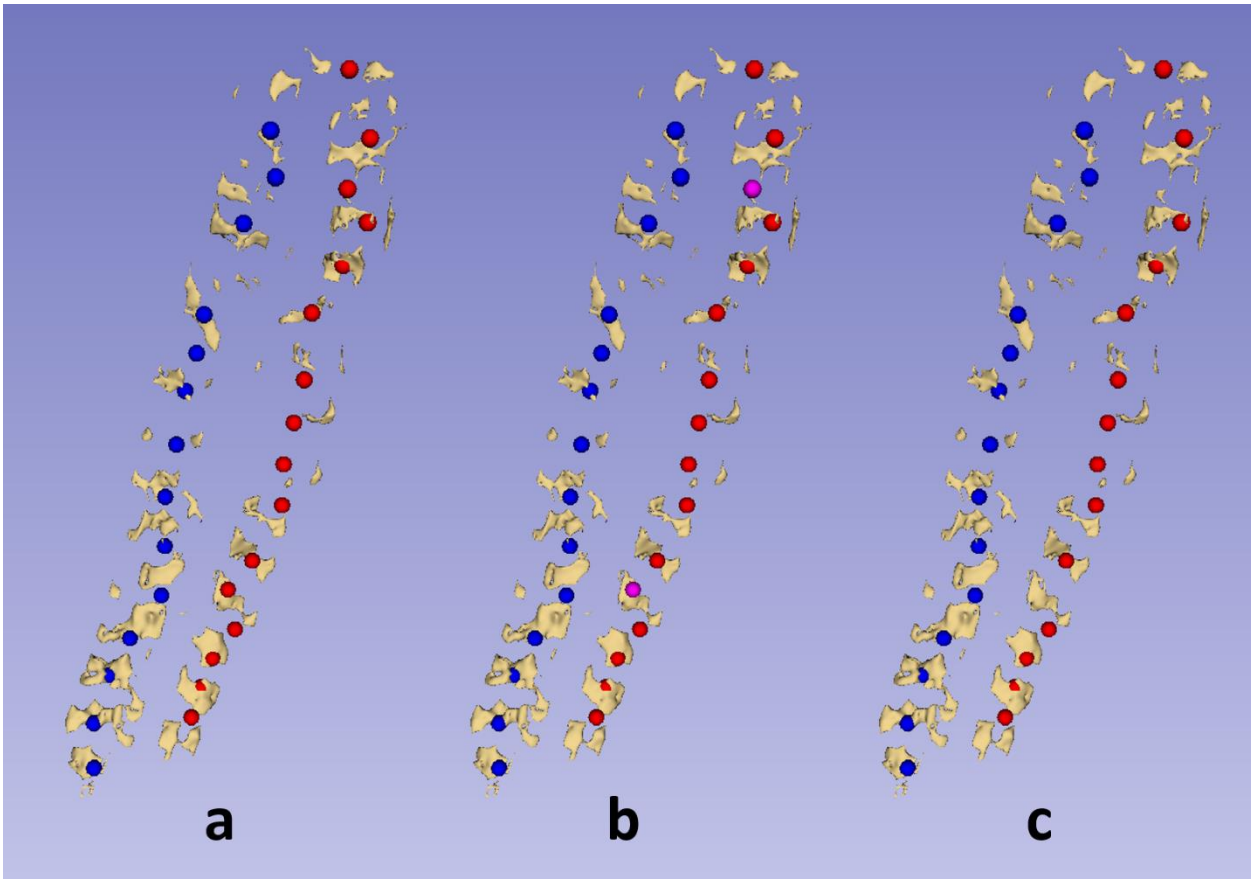


**Figure 37: (a) - Right side is selected after omission imputations (b) - Purple points indicates landmarks identified as outliers (c) - Outlier is removed**

### 4.4 Test cases

Validation of this landmark generation method requires patients with both 3D ultrasound scans and CT or X-ray for validation. Furthermore, the ultrasound scans must be suitable for the segmentation method, meaning the probe should be held in a parasagittal orientation for the scan. This combination of data is unfortunately rare and performing imaging using ionizing radiation is not justified for sole purpose of validating the method. Despite an effective scarcity of available data suitable to validate the collection of techniques presented in this chapter, several test cases were managed. 5 healthy volunteers were recruited for thoracolumbar ultrasound scans. Figure 38 shows the setup used to perform the scans. The ultrasound

machine, monitor, and probe with an embedded electromagnetic position sensor are shown. The reference position sensor and electromagnetic field generator used by the position sensors are also shown.

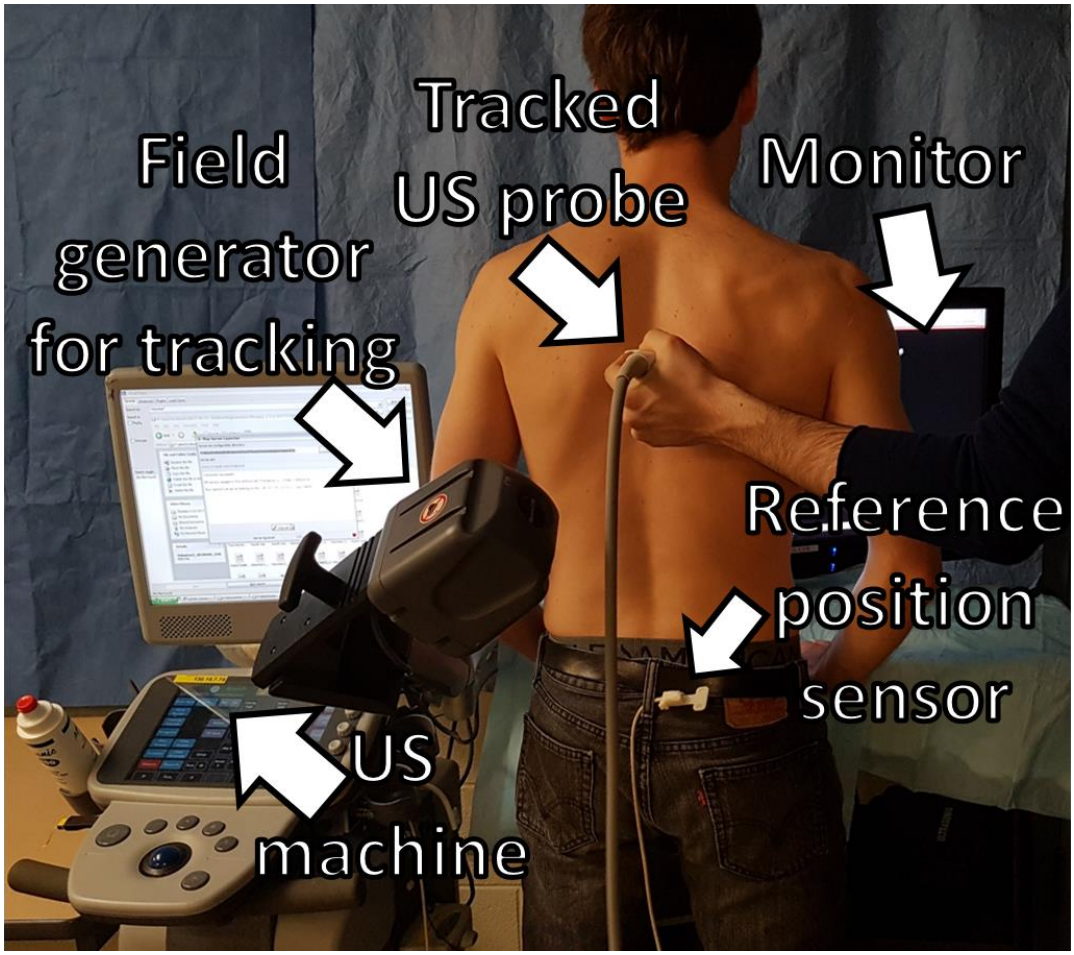


**Figure 38: Setup used to perform test cases**

The probe was held in a parasagittal orientation, as recommended for transverse process imaging. All but one of the reparation operations' parameters, discussed in the previous section and its corresponding subsections, were kept constant for all data processing. In cases where the sparsity of the segmentation resulted in fewer than 5 landmarks being identified on a given side of the spine, the $5^{th}$ degree polynomial was poorly fit to these points because of its higher degree. The user-configurable polynomial degree had to be reduced to accommodate fewer landmarks in two cases. The *k*-means window size was left at 5, and the duplicate detection angle threshold was left at 45°. The omission detection specificity was left at 1, reducing

the threshold for omission detection to the average interval length plus the interval length standard deviation. The patch point count polynomial error reduction threshold was left at -0.1, although this parameter is less important since the user made the final decisions regarding patch point counts, as described above. Finally, the default outlier detection angle threshold of 30° was reduced to 23° for these results. A lower angle was used here to allow use of the same parameters values for each case; a lower number enough angle will detect all outlier, but at the cost of false-positives. These false-positives were re-estimated with omission detection.

Figure 39 shows the major steps the data takes, from ultrasound segmentation to surface visualization. Segmentations are shown once in red, to aid visualization of the sparce data. Although no ground-truth data was availible for validation, the ultrasound segmentations are shown with their resulting visualizations in Figure 40.

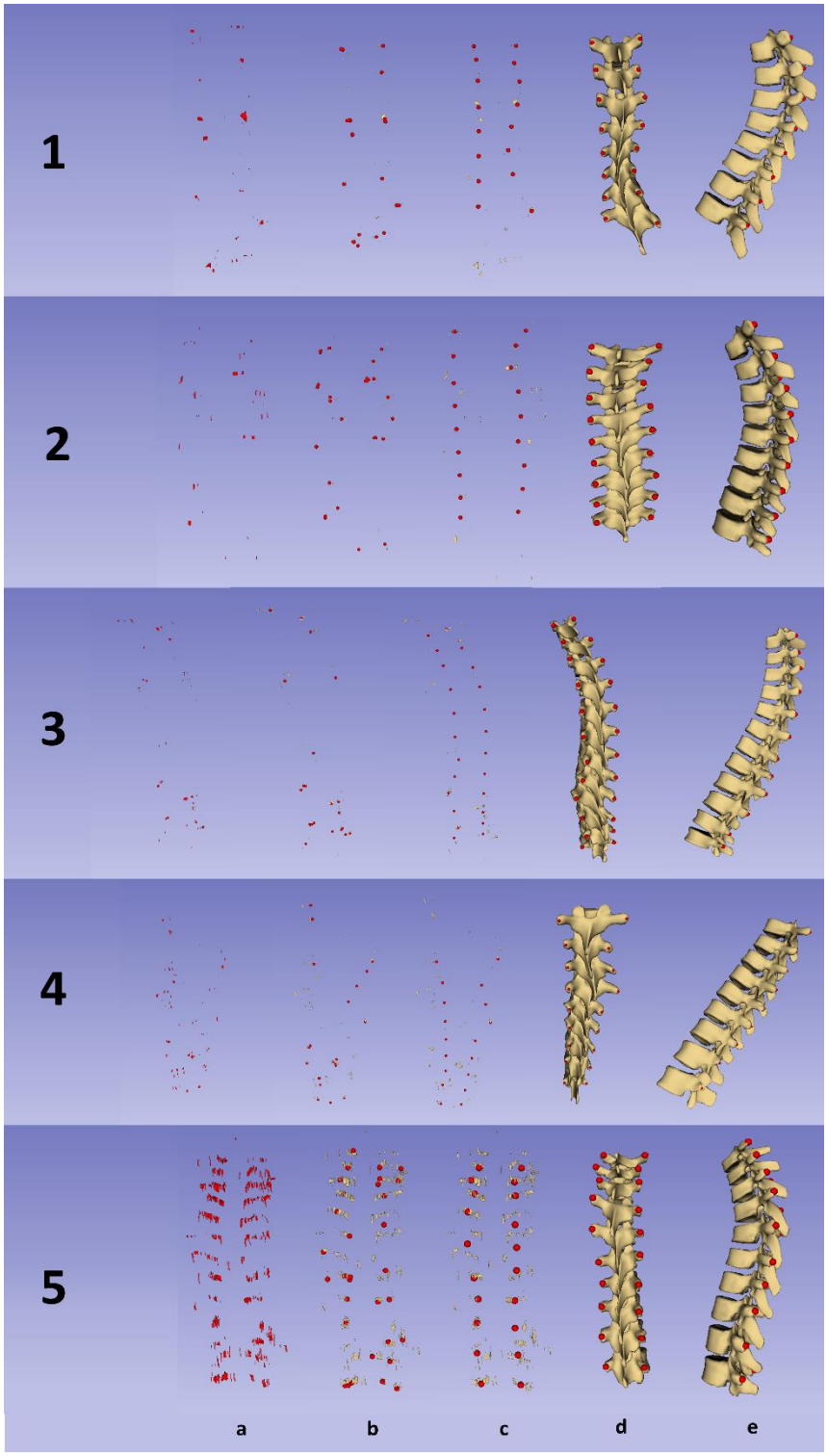


**Figure 39: (a) – Red segmentation of volunteers' ultrasounds (b) - *k*-Means initial estimates of landmark locations as red points on tan segmentations (c) - Landmarks after reparations (d) - Posterior views of subsequent visualizations (e) - Left views of visualizations**

## 4.5 Discussion

The landmark generation method presented in this chapter was tested by generating landmarks from ultrasound segmentations, and generating visualizations from the landmarks for 5 volunteers. Figure 39 shows several steps taken by the data during the process, and Figure 40 shows the segmentations and visualizations, respectively at the beginning and end of the process. The volunteers were healthy; therefore, these results do not indicate the ability of this method to capture the Cobb angle. However, the visualizations can be seen to conform to the parasagittal curvature of the segmentations in Figure 40, right. It is qualitatively apparent from these figures that these visualizations are not the same quality as those of Chapter 3. There are a number of reasons for this.

The segmentations shown in Figure 39a are the starting points from which the first estimates of landmark locations are derived. These segmentations are quite sparse. This sparsity makes the initial landmark location estimates, shown in Figure 39b, inaccurate. They contain many of the types of defects for which reparations have been designed, but they also contain others. The posterior views in Figure 39 and Figure 40 show that the visualizations are often dilated or expanded, particularly towards either end. The reparation operations described above use landmarks above and below defects to test for them and correct them. This means that defects at boundaries of the spine cannot be corrected in the same way. Outliers at the boundaries cannot be removed, imparting the

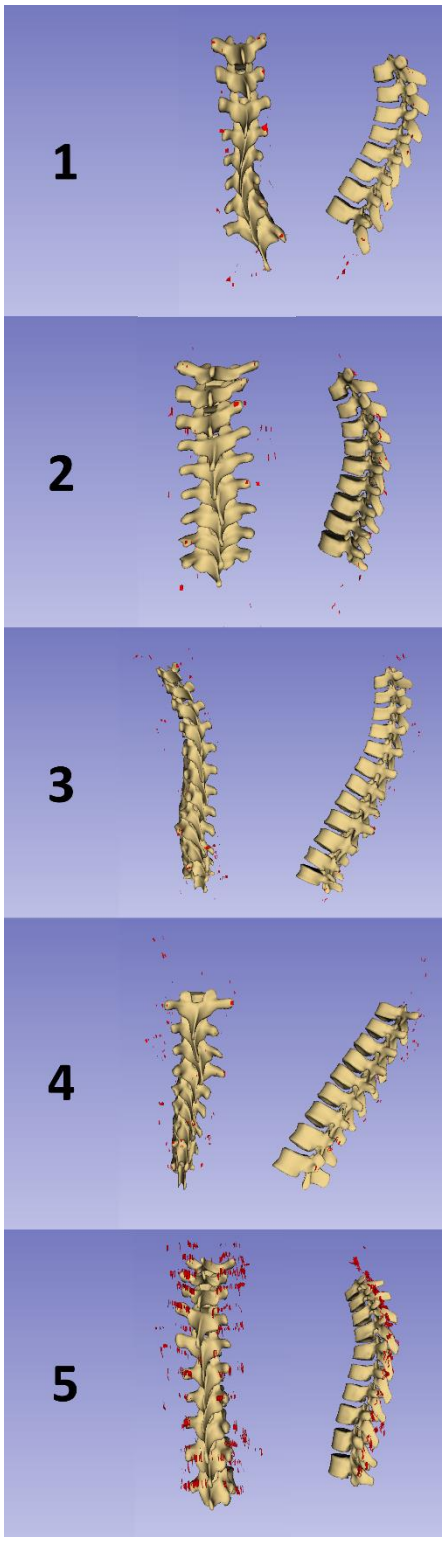


**Figure 40: (Left) - Posterior view of red segmentation and resulting visualization (Right) - Left view**

dilation at the bottom of volunteer #1's visualization and top of volunteer #4's visualization shown in Figure 40. Omissions at the ends of the spine cannot be corrected either. If either side of the spine lacks landmarks at one end, the corresponding landmarks on the other side must be discarded as pair-wise correspondence is required for visualization generation. This accounts for the lengths which the segmentations can be seen to extend beyond the visualizations in Figure 40.

The segmentation method limits the quality of the results when individual landmarks and even vertebral levels are not distinct from one another. Most of the segmentations shown in Figure 40 have one or two vertebral levels with clear bilateral symmetry, and a collection of sparsely distributed small islands. This leaves many of *k*-means' estimates unreliable, and many landmark locations which must be inferred. The segmentation algorithm uses a number of steps, but at a high level, a discernable bright landmark surface, and dark acoustic shadow beneath it must both be present in the image. Figure 41 shows examples of two kinds of ultrasound images which confound the segmentation method. The left image clearly shows the acoustic shadows expected beneath bone, but the absence of a bright surface above them left nothing to segment. The right image shows bright bone surfaces, but without clear acoustic shadows beneath them, they were incorrectly identified as false-positives and removed.

The early stage of development of the segmentation algorithm due to its recent integration into PLUS means that it has not been extensively tested, even outside the context of landmark generation. Work to find ideal default segmentation parameters is ongoing. For example, the edges shown detected in Figure 24d span most of the image. Stricter gradient threshold for edge detection may improve results, provided bones and shadows are both visible. Furthermore, limited time only allowed for the scanning of 5 volunteers. Before even performing a validation study, more scans are required to tune the scanning protocol and parameters. With more time, ultrasound gain, depth, and frequency parameters could have been iteratively tested based on segmentation quality, and improved. Then, for intra and inter-user variability assessment, multiple scans of each could be performed by multiple users.

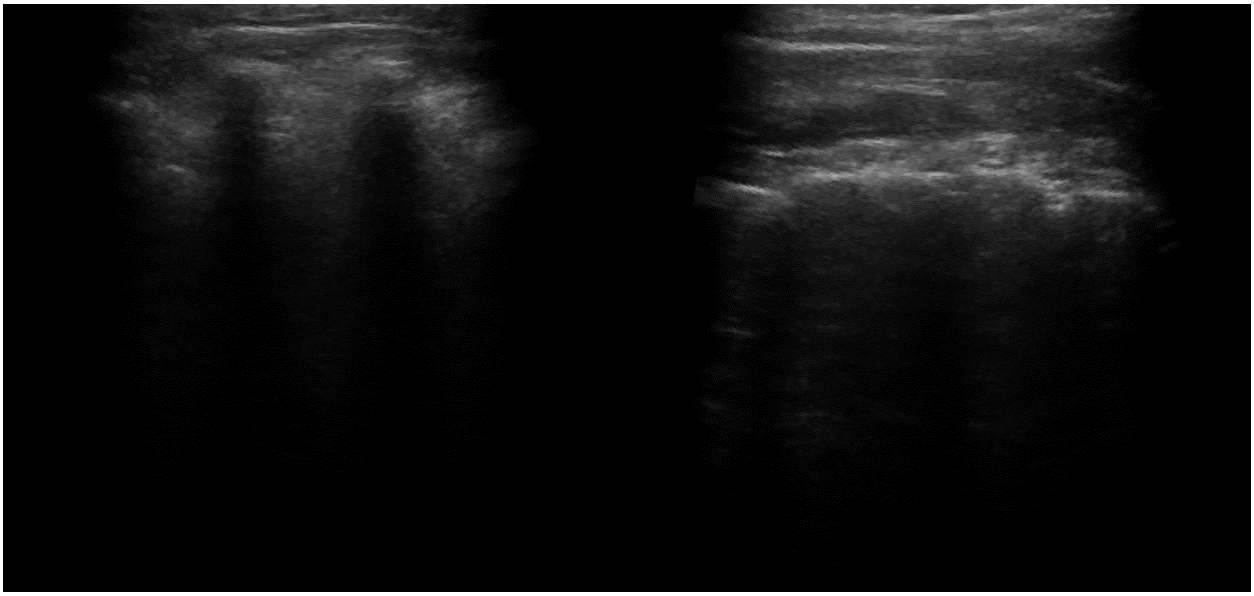

**Figure 41: Two ultrasound images which could not be segmented (Left) - Acoustic shodows visible, but not bone (Right) - Bone visible but not shadow**

The intended purpose of the automatic landmark generation was to reduce the user interaction compared to manually locating landmarks on a series of ultrasound snapshots. Although the reparation operations could be performed simply by clicking buttons, they represent a challenge to be overcome in minimizing user interaction. Typically, one or two iterations of duplicate consolidation were required, numerous patches generated and modified, and outliers removed. For the sake of consistency, the parameters governing the reparation operations were held constant, sometimes at the expense of results' quality. A familiar operator will achieve better results by adapting the parameters to specific data. For example, to find an outlier detection angle threshold low enough to work in each case, false-positives are removed which must be re-estimated, sacrificing patient information. Ideally an operator would set the threshold just low enough to remove only true outliers.

Several improvements to the workflow may be possible, requiring varying degrees of modification to the proposed method. The particular segmentation method used for this workflow [57] was chosen because it was recently integrated into convenient software. It is at an early stage of development and could be replaced with any segmentation method once implemented in PLUS, or as a part of another workflow.

Then, an alternative to the landmark-based method might be used. Landmarks were originally used to correspond to the existing ultrasound based assessment methods. However, reducing a segmentation to a set of landmarks discards information. Registering the healthy-shaped model directly to the segmentation could improve results and reduce processing time. Depending on the quality of the segmentation, geometric or morphological corrections may be required before the registration. Geometric operations can always be developed based on observed defects, but they should not substantially increase user interaction.

### 4.6 Summary

The work presented in this chapter encompasses a possible series of steps to bridge the gap between an ultrasound scan, and the visualizations described in Chapter 3. This bridge was shown in Figure 4, and is highlighted in Figure 42. The method was used to generate visualizations for 5 healthy volunteers as test cases. A lack of CT or X-ray ground-truth prevented rigorous validation of the complete workflow, and limited time prohibited an exhaustive search for optimal scanning parameters. Nonetheless, comparing the visualizations with the segmentations in Figure 40 suggests that patient-specific deformation is still captured to some degree, seen in the anterior-posterior curvature. A better ultrasound segmentation is likely to produce better visualizations in turn. The modular structure of the overall landmark generation method allows another segmentation method to be substituted in. A set of up to 34 landmarks can be a lot to keep track of and difficult to interact with, especially in a repeatable manner. The user-interaction required for the landmark correction methods presents a challenge which must be overcome before full automation is possible. Perhaps the landmarks could be forgone entirely, and the healthy-shaped model registered directly to the segmentation.

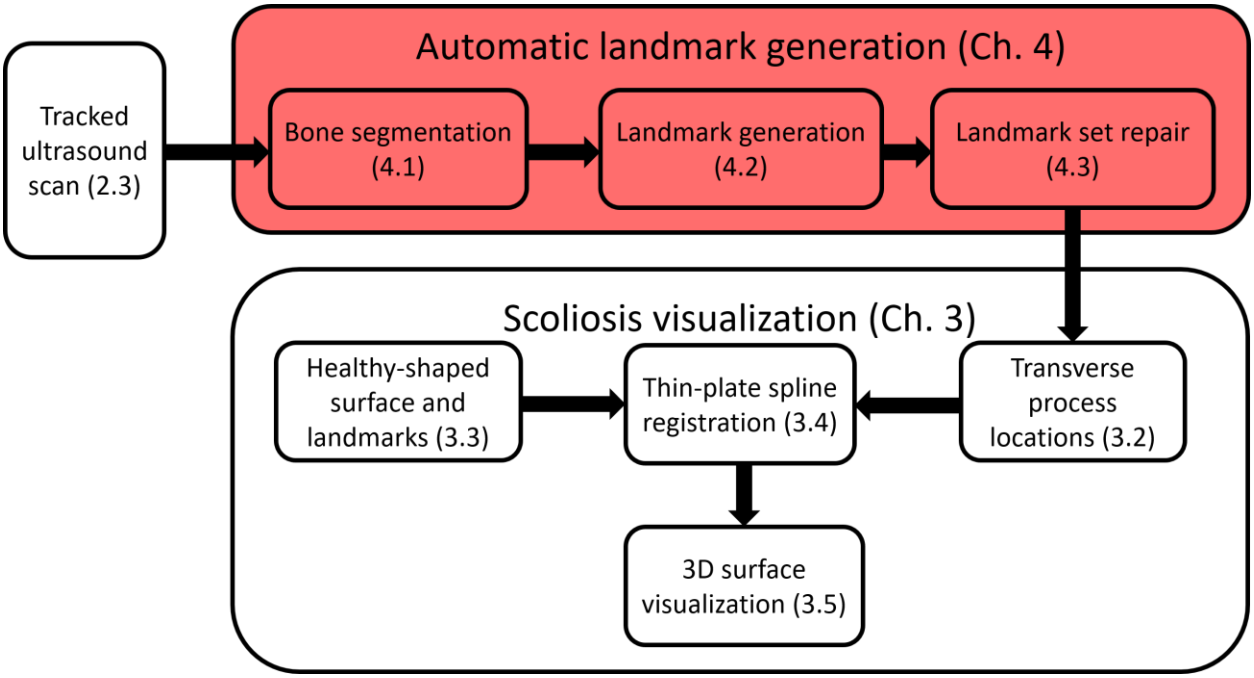


**Figure 42: Position of this chapter's components in the ultrasound to visualization workflow**

# Chapter 5

# Conclusions and future work

The combination of landmark-based visualization method of Chapter 3 and the landmark derivation methods and tools of Chapter 4 enable the workflow that is the overall contribution of this thesis. This workflow is represented by the flowchart in Figure 4. The workflow bridges the gap between scanning, and a realistic 3D spinal visualization, using only ultrasound data. Both the visualization and landmark generation methods are summarized in their respective sections below, with discussion of ongoing and future developments. Finally, conclusions are made with reference to the clinical significance of the work.

## 5.1 Landmark-based visualization method

Chapter 3 described the operation and validation of a method for producing 3D surface visualizations of scoliotic patients' spinal anatomy from ultrasound accessible skeletal landmarks. The method was designed to use landmark locations, because these are what the ultrasound-based scoliosis curvature method use. Results produced to validate the method were generated using transverse process locations identified from 16 scoliotic patients' CTs. CT segmentations were the ground-truths to which the visualization results were compared for quantitative and visual assessment. Generic Hausdorff distance and Dice coefficient registration metrics gave mixed impressions of the results while visual distance maps and Cobb angle reproduction was generally better. These same metrics were recomputed from visualizations generated from landmarks with noise added to their positions. The results were fairly robust with respect to noise, with the average absolute Cobb angle error staying below 5° for small amounts of noise.

Although the landmark-based thin-plate spline registration method produces realistic visualizations of patient specific spinal anatomy, the quantitative validation metrics used were mostly generic, except the Cobb angle error. These generic metrics give a measure of the overall similarity of the visualizations to the ground-truths, whereas some anatomic structures are more important than others, depending on the application. The transverse processes are the only structures for which accuracy is guaranteed, since they

actually have physical landmarks to capture their locations. Injection navigation, for example, is a procedure which would require its own validation of this visualization method. Its validation would likely include measurement of a target registration error, the distances between the facet joints on the visualization and on the ground-truth.

A variation on the visualization method presented in this thesis has been used in work by Baum *et al.* [52]. The visualization method is used to help operators locate skeletal landmarks during an ultrasound scan. After the operator locates a few landmarks, an initial registration is performed, providing an estimation of other landmark locations based on the visualization. As the operator locates additional landmarks, the registration is updated, and the visualization-based estimate is improved. Their study was conducted on a completion time, landmark location rate, and a number of operation-satisfaction questions. The time to completion was higher using the visualization-augmented method, as were landmark identification rates. Users generally liked the system, finding that it was easy to use and helped them located the landmarks.

Although the method for patient-specific spine visualization presented in Chapter 3 was designed to use the transverse process locations as registration landmarks, it is not necessarily limited to the use of these points. The distribution of the transverse processes is the characteristic which makes them suitable for this method. Any set of landmarks with an even number of bilaterally symmetric points per vertebra should result in the necessary anchor point distribution, and an anatomically realistic visualization as output. For example, the articular processes used by Cheung *et al.* [41] or laminae used by Wang *et al.* [42] with different ultrasound protocols might also be suitable. Furthermore, although the method was designed with ultrasound in mind, visualizations could be generated with the landmarks located from other imaging modalities. Although defeating the purpose of eliminating radiation exposure, routine X-ray could benefit from a 3D visualization.

## 5.2 Landmark generation method

Chapter 4 of this thesis presented a method, which used a collection of tools in a Slicer module, to derive a set of transverse process landmarks from an ultrasound segmentation. The motivation for this being that the

time and effort taken to generate a visualization with the method from Chapter 3 could be substantially reduced if the landmarks need not be identified manually. The production of sets of landmarks with bilateral symmetry distributed along the spine from the bone surfaces segmented from ultrasound was demonstrated. The overall workflow was then tested by generating visualizations from these landmarks. The quality of the landmarks and the resulting visualizations depends on the quality of the bone segmentation. Segmentation quality was a function of both the segmentation method and quality of ultrasound images, both with their challenges and opportunities.

The landmark generation method was tested as part of the overall workflow by performing tracked ultrasound scans on 5 volunteers, generating landmarks from the ultrasound scans, and producing visualizations from the landmarks. Rigorous validation of this method will require CT or X-ray ground-truth against which to compare the visualizations, as was done in Chapter 3. In addition to ground-truth, more participants will be required, ideally ones with scoliosis to assess the method's ability to capture deformation. Intra and inter-operator variability should be assessed by having each volunteer undergo multiple scans, and by multiple operators. Similarly to the simulation of noise error in landmark positions for the validation in Chapter 3, more extensive validation of the overall method might be achieved by simulating the kinds of landmark defects addressed in Chapter 4 in accurately located landmarks, and producing visualizations after the appropriate landmark repairs.

A slower ultrasound scan generally results in better data, and can make the difference between an unintelligibly sparse segmentation and a sensible one. This creates a need to balance scanning time with results quality. The scans used to test this method took 3-5 minutes each. The smaller size and better tissue properties of the expected adolescent subjects could reduce the required scanning time, but it could still be challenging for a young patient to remain still for the whole scan. This will be less of an issue if better segmentation can be obtained without slowing down the scanning. A new segmentation method might make use more robust edge detection methods, like local phase symmetry. It may also incorporate the existing method's shadow examination step, designed specifically for transverse process identification. The

requirement of deriving a landmark set from the segmentation is purely the result of the use of landmarks by the presented visualization method. Since reducing a segmentation to a landmark set discards information, visualization results could improve if the healthy-shaped model were registered directly to a segmentation, forgoing landmark points entirely. This would also reduce method complexity and user interaction.

## 5.3 Conclusions

The combination of the landmark-based visualization method of Chapter 3, and the landmark generation method of Chapter 4 is workflow which is the essential contribution of this thesis. This workflow allows users to produce 3D visualizations of scoliotic spines using only ultrasound data. These visualizations are a useful addition to the usual curvature measurement-based scoliotic assessment methods. A chiropractor or physiotherapist, with only ultrasound imaging available, may wish for a better visualization of the patient's anatomy than can be provided with tracked ultrasound images alone. These visualizations could be especially useful for the patients and parents of these care-providers; adolescent patients and their parents are not likely to be as familiar with spinal visualization as a professional. Therefore, these visualizations could help those actually receiving treatment, and their guardians, better understand their own disease. Given that patients typically undergo routine assessment to monitor scoliosis, this method could provide more than a 3D snapshot of the patient's anatomy. Visualizations generated with each assessment, up to several times a year, could demonstrate how the curvature of the spine is progressing, or how it is responding to treatment. These sequential visualizations may also benefit from improved accuracy. The patients' previous visualizations can be updated, rather than new ones produced for each assessment, as they are already closer to the new anatomy to be visualized. Ongoing developments in this work may make it suitable for even more applications. Procedure specific validation could test whether the visualizations can be used intra-operatively, for interventional navigation, for example. The visualization method has also already been adapted to be generated iteratively, helping operators locate the skeletal landmarks used to generate it [52].

# Bibliography


[1] B. Church, A. Lasso, C. Schlenger, D. P. Borschneck, P. Mousavi, G. Fichtinger and T. Ungi, "Visualization of scoliotic spine using ultrasound-accessible skeletal landmarks," in *Proceedings of SPIE*, Orlando, 2017.

[2] M. Konieczny, H. Senyurt and R. Krauspe, "Epidemiology of adolescent idiopathic scoliosis," *J Child Orthop*, vol. 7, p. 3–9, 2013.

[3] F. Altaf, A. Gibson, Z. Dannawi and H. Noordeen, "Adolescent idiopathic scoliosis," *BMJ*, vol. 346, 2013.

[4] S. L. Weinstein, L. A. Dolan, J. G. Wright and M. B. Dobbs, "Effects of Bracing in Adolescents," *The New England Journal of Medicine*, vol. 369, no. 16, pp. 1512-1521, 2013.

[5] S.-Y. Ng and J. Bettany-Saltikov, "Imaging in the Diagnosis and Monitoring of Children with Idiopathic Scoliosis," *The Open Orthopaedics Journal*, vol. 11, pp. 1500-1520, 2017.

[6] L. Kalichman, L. Kendelker and T. Bezalel, "Bracing and exercise-based treatment for idiopathic scoliosis," *Journal of Bodywork & Movement Therapies*, vol. 20, pp. 56-64, 2016.

[7] C. Lehnert-Schroth, "Introduction to the Three-dimensional Scoliosis Treatment According to Schroth," *Physiotherapy*, vol. 78, no. 11, pp. 810-815, 1992.

[8] K. Dobosiewicz, J. Durmala and T. Kotwicki, "Dobosiewicz method physiotherapy for idiopathic scoliosis," *Studies in health technology and informatics*, vol. 135, pp. 228-236, 2008.

[9] K.-D. Kim and P.-N. Hwangbo, "Effects of the Schroth exercise on the Cobb's angle and vital capacity of patients with idiopathic scoliosis that is an operative indication," *J. Phys. Ther. Sci.*, vol. 28, pp. 923-926, 2016.

[10] S. M. Presciutti, T. Karukanda and M. Lee, "Management decisions for adolescent idiopathic scoliosis significantly affect patient radiation exposure," *The Spine Journal*, vol. 14, pp. 1984-1990, 2014.

[11] M. M. Doody, J. E. Lonstein, M. Stovall, D. G. Hacker, N. Luckyanov and C. E. Land, "Breast Cancer Mortality After Diagnostic Radiography," *SPINE*, vol. 25, no. 16, p. 2052–2063, 2000.

[12] H.-R. Weiss and M. Moramarco, "Congenital Scoliosis (Mini-review)," *Current Pediatric Reviews*, vol. 12, no. 1, pp. 43-47, 2016.

[13] K.-J. Cho, Y.-T. Kim, S.-h. Shin and S.-I. Suk, "Surgical Treatment of Adult Degenerative Scoliosis," *Asian Spine Journal*, vol. 8, no. 3, pp. 371-381, 2014.

[14] T. Ailon, J. S. Smith, C. I. Shaffrey, L. G. Lenke, D. Brodke, J. S. Harrop, M. Fehlings and C. P. Ames, "Degenerative Spinal Deformity," *NEUROSURGERY,* vol. 77, no. 4, pp. s75-s91, 2015.

[15] A. Grauers, I. Rahman and P. Gerdhem, "Heritability of scoliosis," *Eur Spine J,* vol. 21, p. 1069–1074, 2012.

[16] US Preventive Services Task Force, "Screening for Adolescent Idiopathic Scoliosis," *JAMA,* vol. 318, no. 2, pp. 165-172, 2018.

[17] J. Deurloo and P. Verkerk, "To screen or not to screen for adolescent idiopathic scoliosis? A review of the literature," *Public Health,* vol. 129, pp. 1267-1272, 2015.

[18] D. Studer, "Clinical investigation and imaging," *J Child Orthop,* vol. 7, pp. 29-35, 2013.

[19] D. Y. T. Fong, C. F. Lee, K. M. C. Cheung, J. C. Y. Cheng, B. K. W. Ng, T. P. Lam, K. H. Mak, P. S. F. Yip and K. D. K. Luk, "A Meta-Analysis of the Clinical Effectiveness of School Scoliosis Screening," *SPINE,* vol. 35, no. 10, p. 1061–1071, 2010.

[20] H. Labelle, S. B. Richards, M. D. Kleuver, T. B. Grivas, K. D. K. Luk, H. K. Wong, J. Thometz, M. Beauséjour, I. Turgeon and D. Y. T. Fong, "Screening for adolescent idiopathic scoliosis: an information statement by the scoliosis research society international task force," *Scoliosis,* vol. 8, no. 17, 2013.

[21] M. Shaw, C. J. Adam, M. T. Izatt, P. Licina and G. N. Askin, "Use of the iPhone for Cobb angle measurement in scoliosis," *Eur Spine J,* vol. 21, p. 1062–1068, 2012.

[22] F. Balg, M. Juteau, C. Theoret, A. Svotelis and G. Grenier, "Validity and Reliability of the iPhone to Measure Rib Hump in Scoliosis," *J Pediatr Orthop,* vol. 34, no. 8, pp. 774-779, 2014.

[23] S.-C. Huang, "Cut-off Point of the Scoliometer in Scholl Scoliosis Screening," *SPINE,* vol. 22, no. 17, pp. 1985-1989, 1997.

[24] P. Cote, B. G. Kreitz, J. D. Cassidy, A. K. Dzus and J. Martel, "A Study of the Dignostic Accuracy and Reliability of the Scoliometer and Adam's Forward Bend Test," *SPINE,* vol. 23, no. 7, pp. 796-803, 1998.

[25] S. Suzuki, T. Yamamuro, J. Shikata, K. Shimizu and H. Iida, "Ultrasound Measurement of Vertebral Rotation in Idiopathic Scoliosis," *J Bone Joint Surg,* Vols. 71-B, pp. 252-255, 1989.

[26] J. M. Frerich, K. Hertzler, P. Knott and S. Mardjetko, "Comparison of Radiographic and Surface Topography Measurements in Adolescents with Idiopathic Scoliosis," *The Open Orthopaedics Journal,* vol. 6, pp. 261-265, 2012.

[27] A. Komeili, L. M. Westover, E. C. Parent, M. Moreau, M. El-Rich and S. Adeeb, "Surface topography asymmetry maps categorizing external deformity in scoliosis," *The Spine Jounal*, vol. 14, pp. 973-983, 2014.

[28] A. Komeili, L. Westover, E. C. Parent, M. El-Rich and S. Adeeb, "Monitoring for idiopathic scoliosis curve progression using surface topography asymmetry analysis of the torso in adolescents," *The Spine Journal*, vol. 15, pp. 743-751, 2015.

[29] A. Komeili, L. Westover, E. C. Parent, M. El-Rich and S. Adeeb, "Correlation Between a Novel Surface Topography Asymmetry Analysis and Radiographic Data in Scoliosis," *Spine Deformity*, vol. 3, pp. 303-311, 2015.

[30] M. C. Tanure, A. P. Pinheiro and A. S. Oliveira, "Reliability assessment of Cobb angle measurements using manual and digital methods," *The Spine Journal*, vol. 10, p. 769–774, 2010.

[31] M. Law, W.-K. Ma, D. Lau, E. Chan, L. Yip and W. Lam, "Cumulative radiation exposure and associated cancer risk estimates for scoliosis patients: Impact of repetitive full spine radiography," *European Jounral of Radiology*, vol. 85, pp. 625-628, 2015.

[32] National Institute for Health and Clinical Excellence, "Diagnostics Assessment Programme - EOS 2D/3D X-ray Imaging System," 2010.

[33] C. McKenna, R. Wade, R. Faria, H. Yang, L. Stirk, N. Gummerson, M. Sculpher and N. Woolacott, "EOS 2D/3D X-ray imaging system: a systematic review and economic evaluation," *Health Technology Assessment*, vol. 16, no. 14, 2012.

[34] H. Eldeeb, N. Boubekri, S. Asfour, T. Khalil and A. Finnieston, "Design of Thoracolumbosacral Orthosis (TLSO) Braces Using CT/MR," *Journal of Computer Assisted Tomography*, vol. 25, no. 6, p. 963–970, 2001.

[35] A. Schmitz, R. Konig, J. Kandyba, P. Pennekamp, O. Schmitt and U. E. Jaeger, "Visualisation of the brace effect on the spinal profile in idiopathic scoliosis," *Eur Spine J*, vol. 14, p. 138–143, 2005.

[36] C. Diefenbach, B. S. Lonner, J. D. Auerbach, N. Bharucha and L. E. Dean, "Is Radiation-Free Diagnostic Monitoring of Adolescent Idiopathic Scoliosis Feasible Using Upright Positional Magnetic Resonance Imaging ?," *SPINE*, vol. 38, no. 7, p. 576–580, 2013.

[37] B. E. Keenan, M. T. Izatt, G. N. Askin, R. D. Labrom, D. D. Bennett, M. J. Pearcy and C. J. Adam, "Sequential Magnetic Resonance Imaging Reveals Individual Level Deformities of Vertebrae and Discs in the Growing Scoliotic Spine," *Spine Deformity*, vol. 5, pp. 197-207, 2017.

[38] K. E. Purnama, M. H. F. Wilkinson, A. G. Veldhuizen, P. M. A. v. Ooijen, J. Lubbers, J. G. Burgerhof, T. A. Sardjono and G. J. Verkerke, "A framework for human spine imaging using a freehand 3D ultrasound system," *Technology and Health Care,* vol. 18, p. 1–17, 2010.

[39] W. Chen, E. H. M. Lou, P. Q. Zhang, L. H. Le and D. Hill, "Reliability of assessing the coronal curvature of children with scoliosis by using ultrasound images," *J Child Orthop,* vol. 7, p. 521–529, 2013.

[40] T. Ungi, F. King, M. Kempston, Z. Keri, A. Lasso, P. Mousavi, J. Rudan, D. P. Borschneck and G. Fichtinger, "Spial Curvature Measurements by Tracked Ultrasound Snapshots," *Ultrasound in Med. & Biol.,* vol. 40, no. 2, pp. 447-454, 2014.

[41] C.-W. J. Cheung, G.-Q. Zhou, S.-Y. Law, K.-L. Lai, W.-W. Jiang and Y.-P. Zheng, "Freehand three-dimensional ultrasound system for assessment of scoliosis," *Journal of Orthopaedic Translation,* vol. 3, pp. 123-133, 2015.

[42] Q. Wang, M. Li, E. H. M. Lou and M. S. Wong, "Reliability and Validity Study of Clinical Ultrasound Imaging on Lateral Curvature of Adolescent Idiopathic Scoliosis," *PLOS ONE,* vol. 10, no. 8, 2015.

[43] D. V. Nguyen, Q. N. Vo, L. H. Le and E. H. M. Lou, "Validation of 3D surface reconstruction of vertebrae and spinal column using 3D ultrasound data – A pilot study," *Medical Engineering and Physics,* vol. 37, pp. 239-244, 2015.

[44] I. Hacihaliloglu, "Ultrasound imaging and segmentation of bone surfaces: A review," *Technology,* vol. 5, no. 2, 2017.

[45] P. Foroughi, E. Boctor, M. J. Swartz, R. H. Taylor and G. Fichtinger, "Ultrasound Bone Segmentation Using Dynamic Programming," in *IEEE Ultrasonics Symposium*, 2007.

[46] J. Kowal, C. Amstutz, F. Langlotz, H. Talib and M. G. Ballester, "Automated bone contour detection in ultrasound B-mode images for minimally invasive registration in computer-assisted surgery – an in vitro evaluation," *Int J Med Robotics Comput Assist Surg,* vol. 3, p. 341–348, 2007.

[47] A. Masson-Sibut, A. Nakib, E. Petit and F. Leitner, "Computer-Assisted Intramedullary Nailing Using Real-Time Bone Detection in 2D Ultrasound Images," in *International Workshop on Machine Learning in Medical Imaging*, 2011.

[48] I. Hacihaliloglu, R. Abugharbieh, A. J. Hodgson and R. N. Rohling, "Bone Surface Localtization in Ultrasound Using Image Phase-Based Features," *Ultrasound in Med. & Biol.,* vol. 35, no. 9, p. 1475–1487, 2009.

[49] I. Hacihaliloglu, A. Rasoulian, R. N. Rohling and P. Abolmaesumi, "Local Phase Tensor Features for 3-D Ultrasound to Statistical Shape+Pose Spine Model Registration," *IEEE Transactions on Medical Imaging,* vol. 33, no. 11, pp. 2167-2179, 2014.

[50] E. M. A. Anas, A. Seitel, A. Rasoulian, P. S. John, D. Pichora, K. Darras, D. Wilson, V. A. Lessoway, I. Hacihaliloglu, P. Mousavi, R. Rohling and P. Abolmaesumi, "Bone enhancement in ultrasound using local spectrum variations for guiding percutaneous scaphoid fracture fixation procedures," *Int J CARS,* vol. 10, p. 959–969, 2015.

[51] F. Berton, C. Farida, M. Marie-Claude and C. Laporte, "Segmentation of the spinous process and its acoustic shadow in vertebral ultrasound images," *Computers inBiologyandMedicine,* vol. 72, p. 201–211, 2016.

[52] Z. Baum, T. Ungi, A. Lasso, B. Church, C. Schlenger and G. Fichtinger, "Visual aid for identifying vertebral landmarks in ultrasound," in *SPIE Medical Imaging*, Houston, 2018.

[53] N. An, "Human spine," GrabCAD, [Online]. Available: https://grabcad.com/library/human-spine-1.

[54] F. L. Bookstein, "Principal Warps: Thin-Plate Splines and the Decomposition of Deformations," *IEEE Transactions of Pattern Analysis and Machine Intelligence,* vol. 11, no. 6, pp. 567-585, 1989.

[55] A. Lasso, T. Heffter, A. Rankin, C. Pinter, T. Ungi and G. Fichtinger, "PLUS: open-source toolkit for ultrasound-guided intervention systems," *IEEE Trans Biomed Eng.,* vol. 61, no. 10, p. 2527–2537, 2014.

[56] F. A., B. R., K.-C. J., F. J., F.-R. J-C., P. S., B. C., J. D., F. F., S. M., B. J., A. S.R., M. J.V., P. S. and K. R., "3D Slicer as an Image Computing Platform for the Quantitative Imaging Network," *Magnetic Resonance Imaging,* vol. 30, no. 9, pp. 1323-1341, 2012 .

[57] S. Kamali, T. Ungi, A. Lasso, C. Yan, M. Lougheed and G. Fichtinger, "Localization of the transverse processes in ultrasound for spinal curvature measurement," in *SPIE Medical Imaging*, Orlando, 2017.

[58] A. Rasoulian, A. Seitel, J. Osborn, S. Sojoudi, S. Nouranian, V. A. Lessoway, R. N. Rohling and P. Abolmaesumi, "Ultrasound-guided spinal injections: a feasibility study of a guidance system," *Int J CARS,* vol. 10, p. 1417–1425, 2015.

[59] D. Behnami, A. Seitel, A. Rasoulian, E. M. Abu Anas, V. Lessoway, J. Osborn, R. Rohling and P. Abolmaesumi, "Joint registration of ultrasound, CT and a shape+pose statistical model of the lumbar spine for guiding anesthesia," *Int J CARS,* vol. 11, p. 937–945, 2016.